Modeling of Gyroklystrons with MAGY

Khanh T. Nguyen, Baruch Levush, *Senior Member, IEEE*, Thomas M. Antonsen, Jr., *Member, IEEE*, Moti Botton, Monica Blank, J. P. Calame, *Member, IEEE*, and Bruce G. Danly, *Member, IEEE*

Abstract—The self-consistent time-dependent code MAGY is presently being used for designing and modeling gyrodevices. In this paper, the code's self-consistent capability is used to investigate three different issues relating to the operation of gyroklystron amplifiers. These are the effect of window reflection on the properties of the output waves, higher order mode excitation in nonlinear output tapers, and excitation in cutoff drift sections. The first two effects can potentially have major impacts on the gyroklystron output radio frequency (RF) in terms of bandwidth power ripple, phase ripple across the band, and mode purity. In fact, strong correlation between simulation results and experimental data indicates that the observed bandwidth ripple in a recently tested W-band gyroklystron can be attributed to a small (-20-dB) window reflection. The last effect, excitation in cutoff drift sections, is found to result in a high level of RF fields at the drive frequency in drift sections. This effect impacts the design and use of lossy ceramics in the drift section because of thermal considerations, particularly in high average power devices.

Index Terms—Gyroamplifiers, gyroklystrons, output tapers, window reflection.

I. INTRODUCTION

DETAILED and accurate nonlinear simulations of the interaction between the electromagnetic (EM) fields and the electron beam in vacuum electron devices are essential to predict their performance. The prediction capabilities are critical to the design and development of future devices. This is the essential impetus for the recent development of the self-consistent, time-dependent, quasi three-dimensional (3-D), new MAGY code [1]. In contrast to the finite-difference–time-domain particle-in-cell (PIC) approach, MAGY employs a reduced description approach in which the EM fields are described by a superposition of the waveguide transverse electric (TE) and transverse magnetic (TM) eigenmodes. Furthermore, the temporal evolution of the EM complex field amplitudes and of the electron beam are assumed to be slow relative to the radio frequency (RF) period, hence, allowing for the averaging over time scales on the order of the RF period. The combination of fast time-scale averaging and the reduced description RF fields substantially reduce the computational

resources compared with that required by PIC codes. However, unlike other reduced description codes, MAGY does not incorporate restricting assumptions on the physics involved and, thus, does not compromise on the fidelity of the results. For instance, in MAGY, the RF field profiles, rather than being restricted to a fixed form, freely evolve in response to the interaction with the electron beam. This capability is achieved via a novel formulation of the generalized telegrapher's equations together with the fast time-scale averaging of the fully relativistic electron equations of motion, which provides for multimode (TE and TM) coupling in arbitrary wall radius profiles, especially at radial step discontinuities. This capability, in single mode form, has previously been discussed in [2]. The new MAGY code is intended for the modeling of both slow- and fast-wave devices. However, in this paper, we shall only report results on a type of fast-wave devices—gyroklystron amplifiers.

Specifically, MAGY is employed to investigate three different effects in gyroklystrons. First is the effect of window reflection on the properties of the output waves. The excellent agreement between experimental data and MAGY simulations strongly suggests that the observed bandwidth power ripple from the recently completed test of a W-band gyroklystron [3], [4] is caused by small power reflections (-20 dB) from the output window. In addition to the power ripple, it can also be shown that reflections introduce ripple on the output phase and modify the effective quality factor of the output cavity across the band. This effect is discussed in Section II. The excitations of higher order modes in the output taper are presented in Section III. The internal mode conversion process inside the output taper provides the initial seed for power in higher order modes, which are then amplified via beam–wave interactions of the gyro traveling-wave–tube type (gyro-TWT) in the uptaper. These interactions can compromise the high mode purity of the output waves for which the taper is designed. Third, Section IV discusses the existence of RF excitation at the drive frequency in cutoff drift sections driven by the bunched electron beam. This phenomenon may impact the design and use of lossy ceramics in drift sections of high-average power devices because of thermal considerations. Section V summarizes and concludes.

II. EFFECT OF OUTPUT WINDOW REFLECTION

It is well established that reflection of microwaves from the output window can influence the performance of gyrotron oscillators [5]–[9]. Small window reflections can result in mode competition and frequency jumping in these devices. In gyroamplifiers, window reflections are responsible for the power ripple
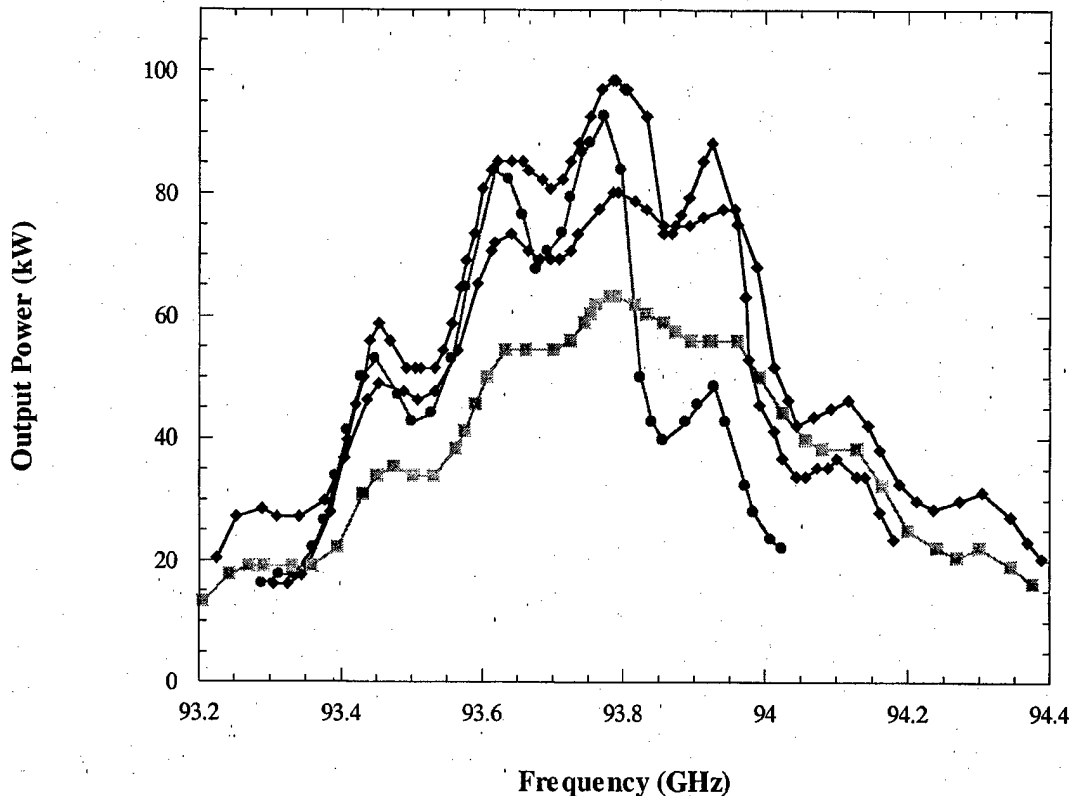
Fig. 1.   Experimental bandwidth plots of the high average power W-band gyro-klystron at four different magnetic field settings. Beam current and voltage are 4 A and 65 kV, respectively.

across the bandwidth of the high-average power W-band gy-roklystron amplifier [3], [4]. The experimentally observed band-width ripple is illustrated in Fig. 1 for four different circuit mag-netic fields. The beam current and voltage for the cases shown are 4 A and 65 kV, respectively. As shown in Fig. 1, the peaks and valleys of the ripple occur at constant frequencies for all four magnetic fields. Similar behavior has also been observed at all beam currents. The modulation of the gyroklystron fre-quency response seen in Fig. 1 is indeed surprising, especially considering that the reflected power is at least 20 dB down from the outgoing RF waves according to window cold tests. In this section, we shall first discuss a simple analytical model, which describes the effect of window reflection on gyroklystron ampli-fier performance. The resulting scaling laws are then compared with MAGY simulation results. This section concludes with a detailed comparison of MAGY results with experimental data.

The Naval Research Laboratory (NRL)/Litton/Communica-tion and Power Industries' (CPI) high-average power W-band gyroklystron amplifier is a stagger-tuned four-cavity TE01 gy-roklystron operating at the fundamental cyclotron harmonic [3], [4]. The amplifier geometry is illustrated by Fig. 2, which shows the four cavities and the nonlinear output uptaper (∼10.1 cm in length). The cavities are isolated from each other by drift sec-tions, which are cutoff to the operating mode. Following the up-taper is the collector, which also serves as the RF output wave-guide [10]. At the end of the collector (∼63.6 cm downstream from the end of the uptaper) is a single-disk chemical vapor deposition (CVD) diamond window. As alluded to earlier, this
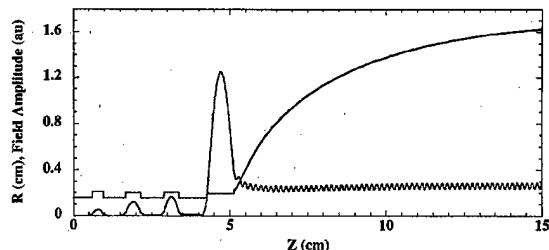

Fig. 2.   Geometry and a typical RF field profile from MAGY simulations of the high average power W-band gyroklystron. A window reflection of −20-dB has been assumed.

window has been cold-tested and found to have a return loss of approximately −20-dB reflection (1% power reflection) over the frequency range of interest. Also shown in Fig. 2 is a typical RF field profile simulated with MAGY with a −20-dB window reflection. This field profile has two particular noteworthy fea-tures. One is the standing wave pattern seen in the nonlinear uptaper, which results from the interference between the for-ward going wave and the backward-reflected RF. The other is the presence of finite RF amplitude in the cutoff drift section between the penultimate and the output cavities. This shall be the topic of discussion in Section IV.

In gyroklystrons, an annular gyrating electron beam, usually produced with a magnetron injection gun (MIG), is introduced into the interaction circuit, which comprises of at least two cav-ities. At the input cavity, the electron energies are modulated by
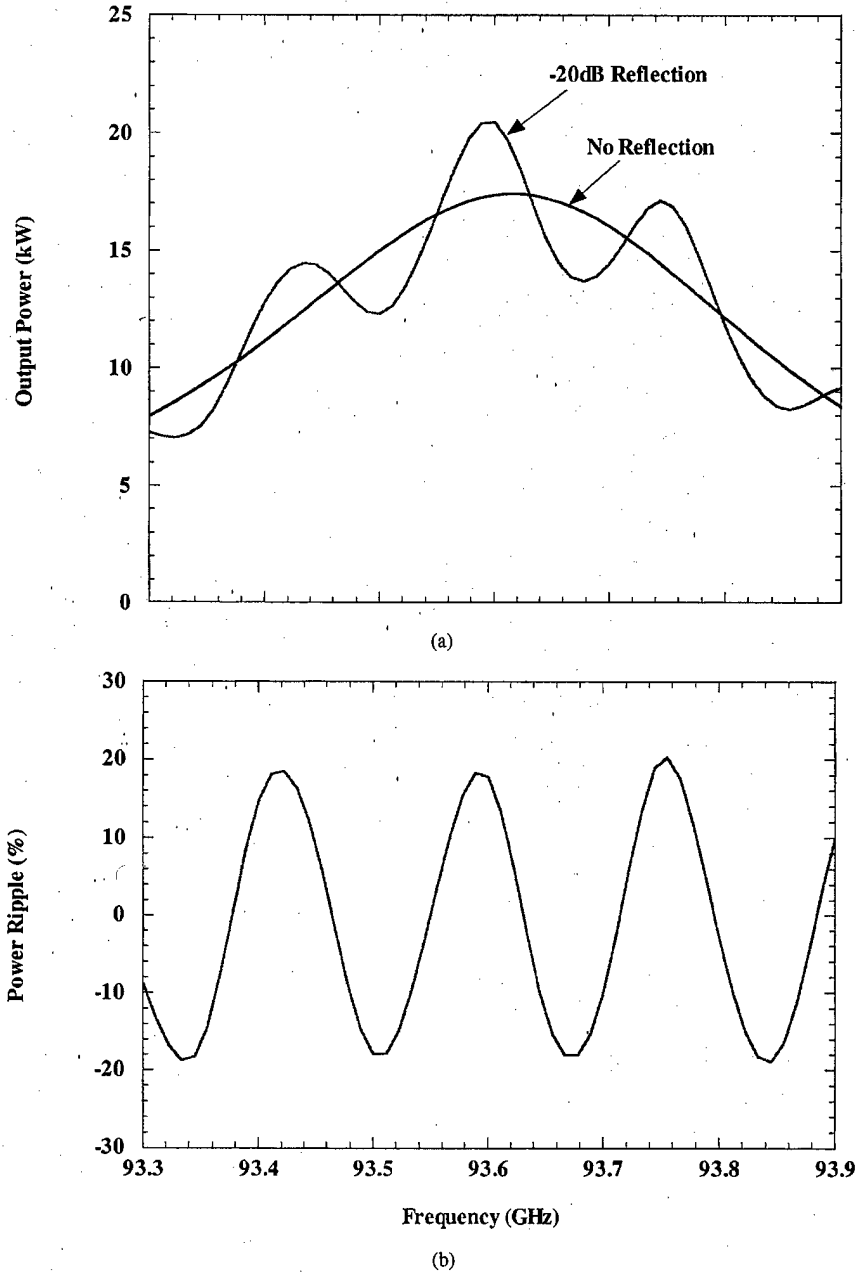
(a)

Frequency (GHz)

(b)

Fig. 3. (a) Output power versus frequency with and without window reflection and (b) corresponding power ripple, $\Delta P/P_0$, for constant RF current source excitation of output cavity.

the TE fields introduced by the RF input power, changing their relativistic cyclotron frequencies. The modulation of relativistic cyclotron frequencies causes the electrons to bunch in phase angle. The azimuthal bunching process is further enhanced via ballistic bunching in the drift sections and by the intermediate cavities. Finally, the RF power is diffractively coupled from the output cavity and flows toward the output window. In steady state, energy balance dictates that power extracted from the electrons must equal the RF power diffractively coupled from the cavity plus the ohmic power lost inside the cavity. Assuming negligible ohmic loss, the above statement can be expressed as

$$P_{\mathrm{out}}(\omega) = \frac{\omega}{Q_{\mathrm{diff}}} W(\omega) = \int_V \vec{E}_{\mathrm{RF}}(\omega, \vec{r}) \cdot \vec{J}_b(\omega, \vec{r}) \, dV. \quad (1)$$

Here, $\omega = 2\pi f$ is the angular frequency of the input power. Q_{diff} is the diffractive quality factor of the output cavity. E_{RF} is the cavity RF electric field. J_b is the electron bunching current density at frequency ω and a function of the RF electric field, and W is the output cavity stored energy. The stored energy is given by

$$W(\omega) = \frac{\varepsilon}{2} \int_V \vec{E}_{\mathrm{RF}}(\omega, \vec{r}) \cdot \vec{E}_{\mathrm{RF}}^*(\omega, \vec{r}) \, dV \quad (2)$$

where the integral is over the output cavity volume.

It is worthwhile to note at this juncture that the output window reflection will only influence the output cavity because the cavities are isolated from one another by the drift sections. Defining $E_{\mathrm{RF}} = E_0$ as the output cavity RF electric field without window

reflection, the cavity electric field with finite reflection coefficient, ρ, can be expressed as

$$\vec{E}_{\mathrm{RF}} = \vec{E}_0(1 + R)\{1 + R + R^2 + \cdots + R^N\} \qquad (3)$$

where $R = \rho e^{i\phi}$ is the complex reflection coefficient and ϕ is the total phase shift for the round-trip time from the cavity to the window and back. This phase shift is given by [6]

$$\phi(\omega, L) = \phi_r + 2 \int_0^L k_z(\omega, z) \, dz \qquad (4)$$

where ϕ_r is the phase shift induced by the window, k_z is the axial wavenumber, and L is the distance between the output cavity and the window (including the nonlinear output taper).

In (3), the geometric series represents the contribution from previous reflections. Because $\rho < 1$, this series quickly converges and we obtain

$$\vec{E}_{\mathrm{RF}} = \vec{E}_0 \left(\frac{1 + R}{1 - R} \right). \qquad (5)$$

In the event that J_b is weakly dependent or independent of E_{RF} (e.g., linear regime), it follows from (1) that

$$P_{\mathrm{out}}(\omega, L) \cong P_0(\omega, L) \, \mathrm{Re} \left(\frac{1 + R}{1 - R} \right)$$
$$= P_0 \left(\frac{1 - \rho^2}{1 + \rho^2 - 2\rho \cos\phi} \right) \qquad (6)$$

where P_0 is the output power without reflection. Because ϕ is a function of ω, a bandwidth power ripple on the order of

$$\left(\frac{-2\rho}{1 + \rho} \right) \leq \frac{\Delta P}{P_0} \leq \left(\frac{2\rho}{1 - \rho} \right) \qquad (7)$$

can be expected. Using the waveguide dispersion relation for the region between the output cavity and window, the ripple frequency spacing is found from (4) to be

$$\Delta f(\omega, L) = \frac{c^2}{\int_0^L \frac{2\omega \, dz}{k_z(\omega, z)}} = \frac{c^2}{\int_0^L \frac{2 \, dz}{v_g(\omega, z)}} \qquad (8)$$

where v_g is the group velocity. Thus, for example, we can expect a bandwidth power ripple of approximately ±20% for a −20-dB ($\rho = 0.1$) reflection. As previously mentioned, (7) is valid only when J_b is weakly dependent on or independent of E_{RF}, such as near the band edges or in the linear regime where the efficiency is low. At, or near saturation, strong interaction with the RF fields rapidly depletes the electron-beam transverse kinetic energy. Consequently, variation of the RF fields will have a weaker impact on the output power level (well known in amplifiers as gain suppression); hence, (7) only serves as an upper limit for the power ripple.

To study the impact of window reflection on gyroamplifiers self-consistently, a window reflection model has been implemented in MAGY. In order to test this model and to validate (7) and (8), MAGY simulations are first performed by exciting the output cavity with a constant RF current source (without an
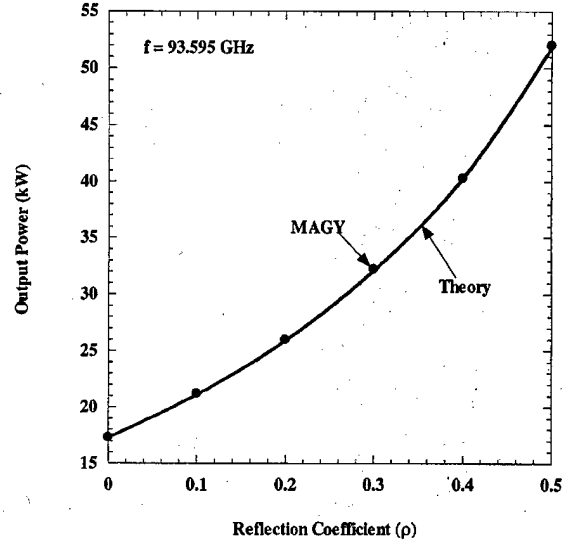

Fig. 4.   MAGY output power versus reflection coefficient (dots) and expected output power according to (6) at the fixed frequency of 93.595 GHz for constant current excitation of output cavity.

electron beam). The source has a Gaussian axial profile. This is the technique to determine the cold-cavity resonance frequency and cavity quality factor (Q) in MAGY. Shown in Fig. 3(a) are the output powers versus frequency with $(-20 \, \mathrm{dB})$ and without window reflection. The power curve without reflection shows the output cavity cold resonance frequency to be 93.62 GHz with a -3-dB bandwidth of 0.567 GHz corresponding to Q_{diff} = 165. More illustrative is Fig. 3(b), which shows the power ripple $(\Delta P/P_0)$ versus frequency for the two power curves in Fig. 3(a). The ripple amplitude is approximately ±20%, as expected from (7). The ripple spacing, Δf, is 0.17 GHz and is consistent with (8) for $L \approx 73.6$ cm (including the nonlinear uptaper shown in Fig. 1). The scaling of output power versus reflection coefficient, ρ, at a fixed frequency is illustrated in Fig. 4 for both MAGY simulations and (7) with excellent agreement. The frequency for this particular case is 93.595 GHz, which corresponds to $\phi = 0$, as can be inferred from Fig. 3. We note here that MAGY simulations do not model the device all the way to the output window, which is computationally intensive. It is only necessary to induce a reflection at the end of the simulation, which properly accounts for the window reflection coefficient, the delay time, and the phase shift introduced by the waveguide in accordance with (4). For the case at hand, the end of the simulation is also the end of the uptaper, as illustrated in Fig. 2.

Recall from (1) and (2) that although the output power is approximately proportional to E_{RF}, the cavity stored energy is proportional to $|E_{\mathrm{RF}}|^2$. Thus, the cavity stored energy with reflection is given by the stored energy without reflections, W_0, by

$$W(\omega, L) = W_0(\omega) \left(\frac{1 + \rho^2 + 2\rho \cos\phi}{1 + \rho^2 - 2\rho \cos\phi} \right). \qquad (9)$$

This scaling is borne out by Fig. 5, which shows the cavity stored energy with and without reflection corresponding to the cases shown in Fig. 3. The main implication of the scaling given by (7) and (9) when taken together is the modification of the output
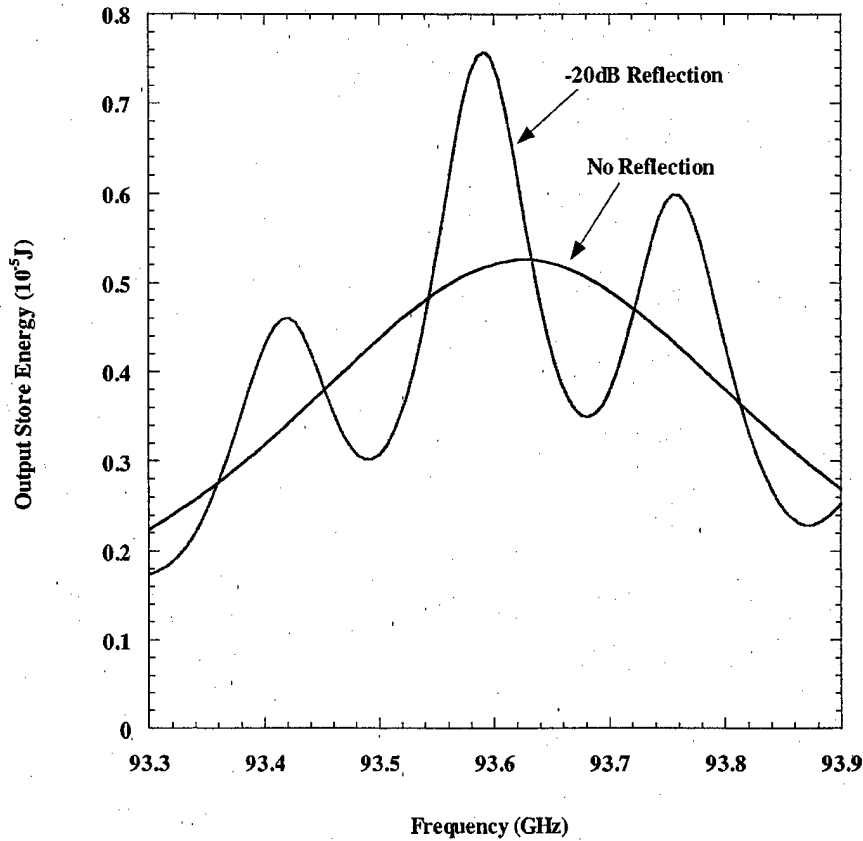
Fig. 5.   Output cavity stored energy versus frequency corresponding to the constant current excitation case shown in Fig. 3.

cavity diffractive quality factor Q_{diff}. Consequently, in the presence of reflection the effective cavity quality factor, Q_{eff}, is given by

$$Q_{\text{eff}}(\omega, L) = \frac{\omega W(\omega, L)}{P_{\text{out}}(\omega, L)}$$
$$= Q_{\text{diff}} \left(\frac{1 + \rho^2 + 2\rho \cos \phi}{1 - \rho^2} \right) \qquad (10)$$

which is a function of both frequency and reflector position. This implies that small reflections can significantly impact the start oscillation current threshold of the output cavity in gyroklystrons.

In addition to causing bandwidth power ripple, window reflections also induce a ripple in the output phase across the band relative to the output phase without reflections. It can be expected from the above discussions that the relative output phase ripple induced by reflection, $\Delta \varphi$, will be identically zero at the peaks and valleys of the bandwidth power ripple (where $\phi = n\pi, n = 0, 1, 2, 3 \cdots$ etc.). The relative output phase ripple will be at a maximum or a minimum when the round-trip phase shift is $\phi = n\pi/2, n = 1, 3, 5 \cdots$ etc. At these points, assuming the current source is independent of E_{RF}, such as in the constant current source excitation, the reflected wave does not interact with the current source in the cavity and is simply reflected back to the output waveguide. From power balance considerations, the relative output phase is

$$\Delta \varphi(\omega, L) = \text{Atan} \left(\frac{\rho \sin \phi}{(1 - \rho^2)^{1/2}} \right). \qquad (11)$$

The output phase versus frequency corresponding to the cases shown in Fig. 3 from MAGY simulations is plotted in Fig. 6(a). The difference between the output phase with and without window reflection is shown in Fig. 6(b). The relative output phase ripple of ± 0.1 radians is consistent with (11). However, in the case when the current source is dependent on the cavity RF fields, the electron bunching current can undergo a phase shift and interacts with the reflected wave. In this case, the maximum magnitude of the relative output phase can be estimated from (5) to be

$$|\Delta \varphi_{\text{max}}| \leq \text{Atan} \left(\frac{2\rho}{1 - \rho^2} \right). \qquad (12)$$

In other words, an output phase ripple of up to ± 0.2 radians can be expected for a -20-dB reflection.

Thus far, MAGY simulation results have only been shown for the constant RF current excitation of the output cavity. To illustrate the influence of window parameters on the performance of gyroklystrons, we have also performed MAGY simulations of the four-cavity W-band gyroklystron with electron beams. The main difference, with respect to the constant current source cases, are that electron beams enter the output cavity prebunched under the influence of the previous three cavities and that the bunched electron current can be further modulated by the output cavity RF fields. Shown in Fig. 7(a) is the MAGY simulated bandwidths plot for a 6-A, 65-kV electron beam at saturation with and without reflection. More details about the device will be discussed in later paragraphs and can also be
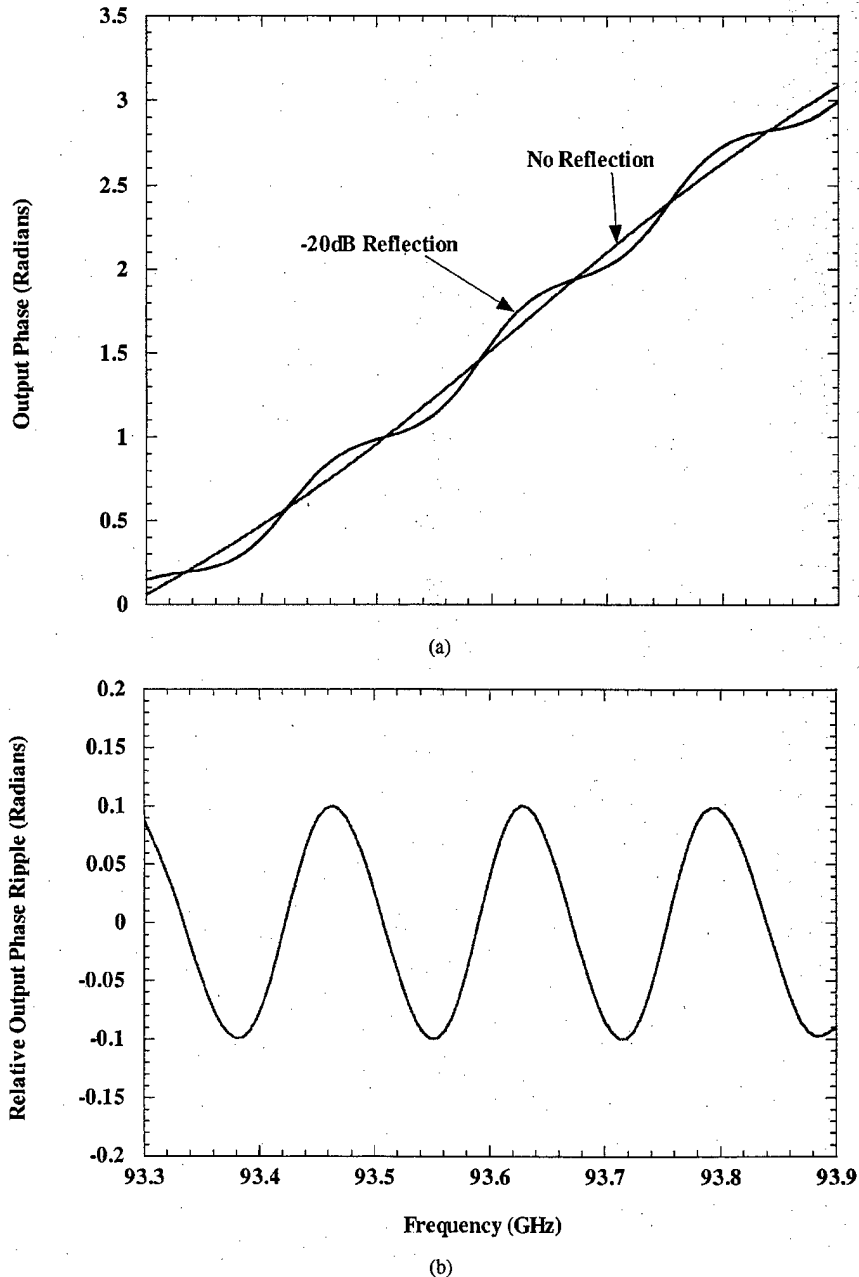
Fig. 6.   (a) Output phase versus frequency with and without window reflection and (b) corresponding relative phase ripple, $\Delta\varphi$, for constant RF current source excitation of output cavity [Fig. 3].

found in [3] and [4]. For these simulations, the beam pitch angle ($\alpha = v_\perp/v_z$) is 1.22 with no velocity spread and the magnetic field is 36.4 kG with a -1% taper over the circuit. Note that the center frequency shown in this plot is now 93.84 GHz, reflecting an upshift of 220 MHz from the cold resonance frequency of 93.62 GHz [Fig. 3], because of the effect of beam loading. As previously mentioned, the window is $\sim$73.6 cm from the output cavity with a -20-dB reflection. The power ripple is plotted in Fig. 7(b). In contrast to Fig. 3(b), when the output cavity is excited with a constant RF current source, the ripple magnitude here is less than 20% and is much larger at the band edges than at the center. This effect has been previously explained in the discussion following (7). The output phase for this case is plotted

in Fig. 8(a), and the relative output phase ripple is shown in Fig. 8(b). As expected, the maximum magnitude of the phase ripple is larger here than that shown in Fig. 6(b), but is less than 0.2 radians, as can be expected from (12). Note that the frequency spacing between ripples is the same as in the constant current excitation case, as expected.

The dependence of the bandwidth ripple on the length between the output cavity and the window is illustrated by Fig. 9 for two different lengths $L = 40$ and 130 cm. The simulation parameters are exactly those described in the previous paragraph. Comparing with Fig. 7(a), it can be seen that the frequency spacing is larger (smaller) for shorter (longer) lengths in accordance with (8). In addition, the frequency at which the peaks
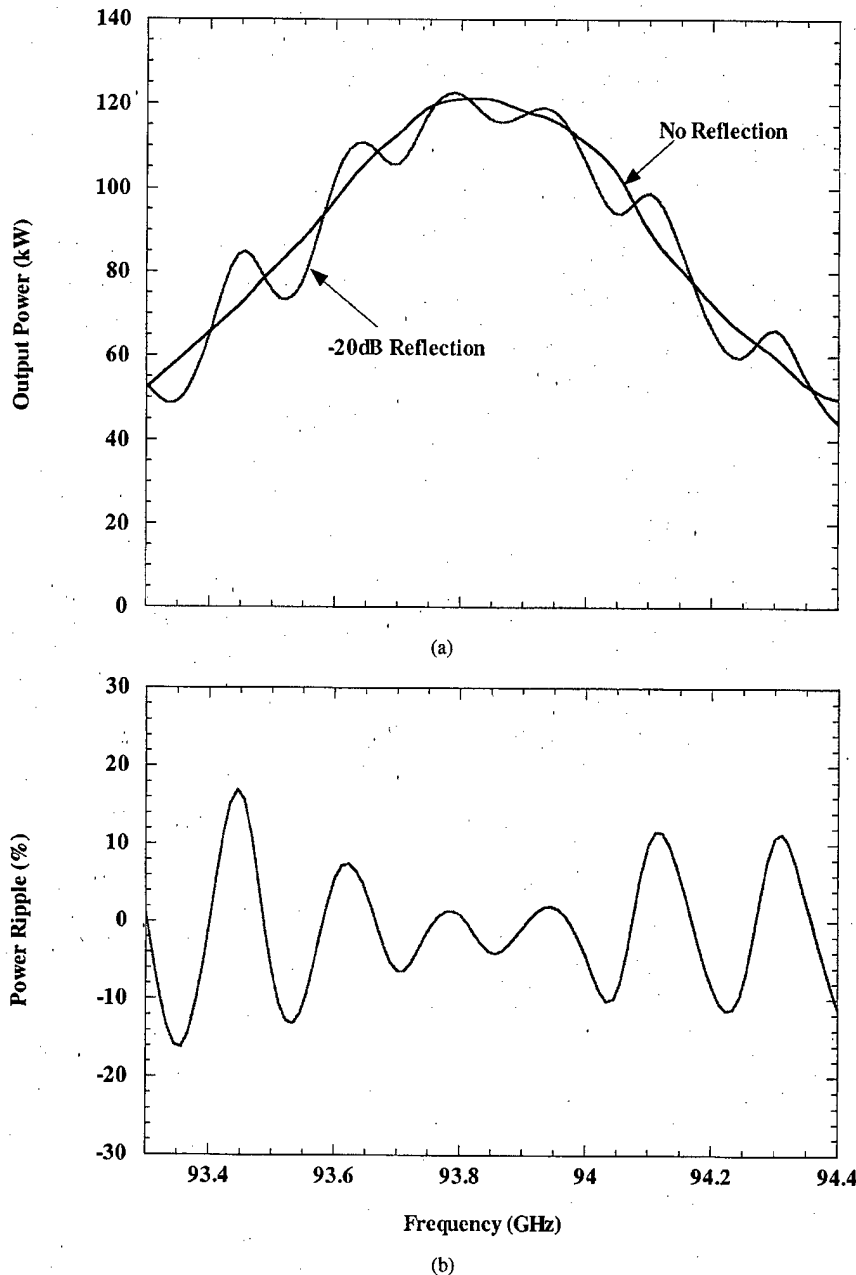
(a)

(b)

Fig. 7.   (a) Saturated bandwidth with and without window reflection and (b) corresponding power ripple, $\Delta P/P_0$, for a 6 A, 65 kV, $\alpha = 1.22$ electron beam. Beam enters output cavity prebunched due to interactions in the three previous cavities.

and valleys of the bandwidth ripple occur is also extremely sensitive to the position of the window. This is demonstrated in Fig. 10 for two window positions, one-quarter of an axial wavelength apart ($\sim$0.8 mm). The interchange between peaks and valleys can clearly be seen. This behavior is apparent upon inspection of (4) and (6). Dependence of bandwidth ripple on the reflection levels is shown in Fig. 11 for -20-dB [Fig. 6] and -26-dB reflections. As expected, the ripple magnitude is lower for smaller reflections.

In order to confirm that window reflections are indeed the cause of the experimentally observed bandwidth ripples, as illustrated in Fig. 1, a series of MAGY simulations have been performed for direct comparison with the data using known experimental parameters from the four-cavity W-band gyroklystron experiments [3], [4]. The resonance frequency and quality factor for each of the four cavities in the simulations are tuned within the experimental uncertainty of the cold-test measurement [11]. The simulated geometry of this amplifier is illustrated in Fig. 2. The beam pitch angles and velocity spreads used in the simulations are extrapolated from EGUN [12] simulations of the MIG [10]. The extrapolation is based on experimental start-oscillation data and MAGY-predicted pitch angle for the output cavity oscillation threshold, and on the relative change of gun voltages and magnetic field settings used in these experiments.
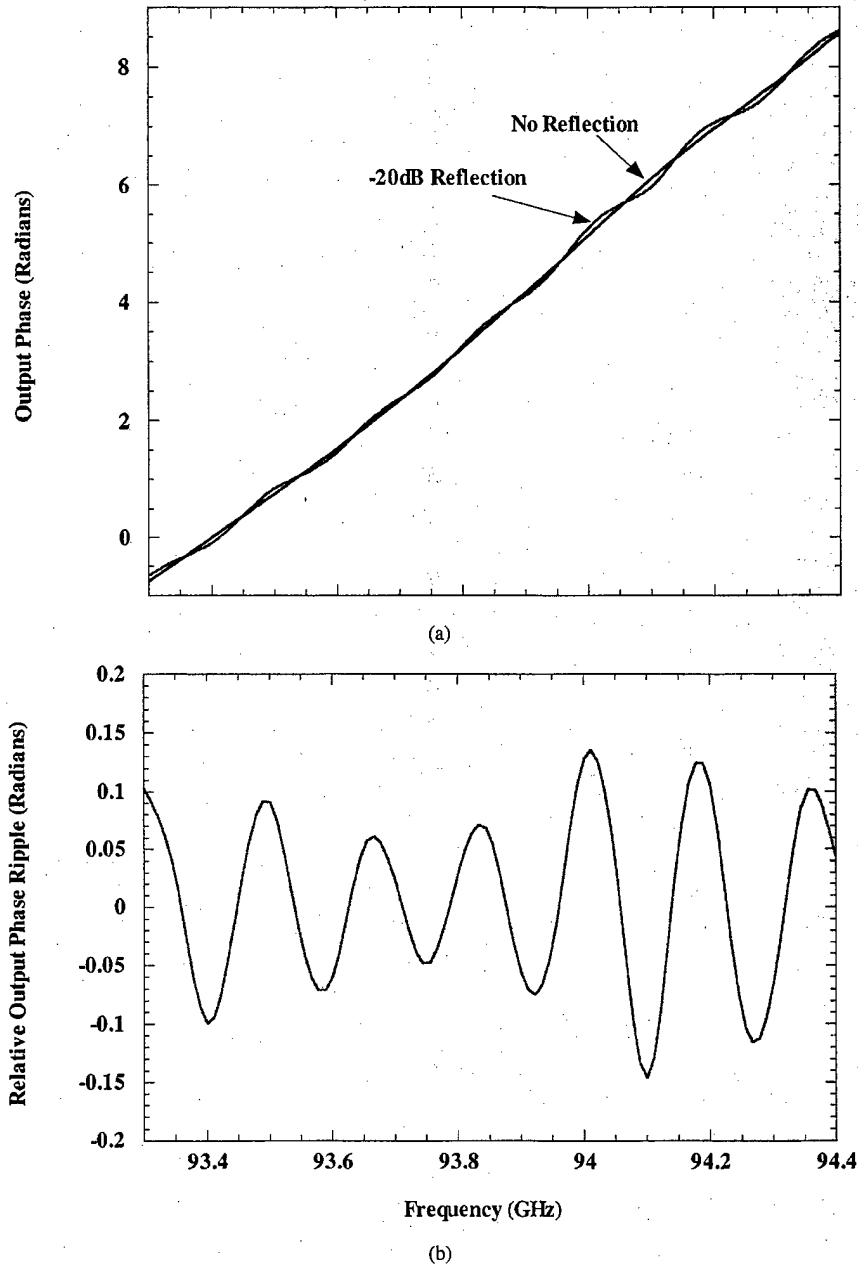
(a)

(b)

Fig. 8.   (a) Output phase versus frequency with and without window reflection and (b) corresponding relative phase ripple, $\Delta\varphi$, for a 6 A, 65 kV, $\alpha = 1.22$ electron beam [Fig. 7].

The gun and interaction circuit magnetic field are calculated with the magnetics code EFFI [13] using the experimental current settings and the superconducting coil dimensions as input. Measured and calculated magnetic field profiles are in excellent agreement. Most importantly, a window located $\sim$73.6 cm (according to the design) from the output cavity with a reflection of -20 dB (window cold-test value) is assumed in all simulations.

Shown in Figs. 12 and 13 are comparisons of MAGY simulated and experimentally measured saturated bandwidths and drive curves, respectively, at four different magnetic fields for 4-A, 65-kV electron beams. The agreement between measured data and simulated results is very good. The beam pitch angle and transverse velocity spread used for each case is as shown in the plots, as are the input power for the bandwidth and the drive frequency for the drive curves. Note that the input power given here is from the measured power at the input cavity flange, which includes the $\sim$3-dB loss between this flange and the TE_{01} cavity. The axial magnetic field profile employed in the simulations is shown in Fig. 14, as calculated using EFFI. Similar simulation/measurement agreement is also obtained for bandwidth and drive curves with 6-A, 65-kV electron beams at four magnetic field profiles, as illustrated by Figs. 15 and 16, respectively. The corresponding magnetic field profiles are as shown in Fig. 17.
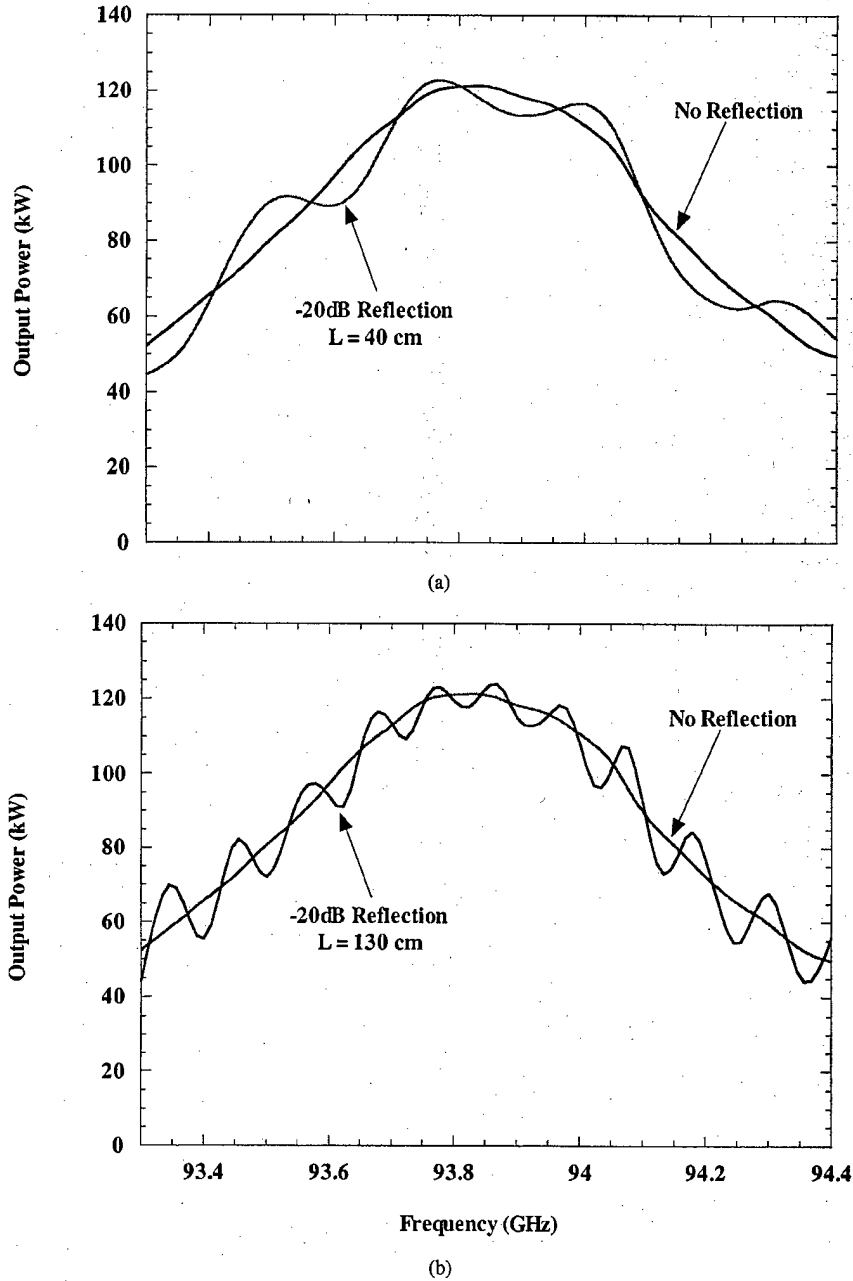
Fig. 9. Saturated bandwidth plots with and without reflection of a 6 A, 65 kV, $\alpha = 1.22$ electron beam as in Fig. 7 but for two different distances between window and output cavity (a) $L = 40$ cm and (b) $L = 130$ cm.

The good agreement between simulation and the experiment demonstrated here, together with the absence of bandwidth ripple in simulations with no reflection, strongly suggests that window reflections are indeed the cause of the observed bandwidth ripple in the high-average power W-band gyroklystron. In addition to the bandwidth ripple, window reflections also induce output phase ripple, as discussed earlier. Even though the discussion given here has been restricted to window reflection, the analysis is general and can be applied to other types of reflectors. Moreover, we have shown that, similar to the large signal code MAGYKL [14], MAGY can be used for designing gyroklystrons. In particular, MAGY application is required for describing self-consistent effects. This is the topic of the next two sections.

III. HIGHER ORDER MODE EXCITATION IN OUTPUT TAPER

High-average power gyroamplifiers often employ an output taper to transition from the near-cutoff dimensions of the interacting circuit to a larger dimension waveguide [15]. This transition is necessitated by thermal considerations of the spent-beam collectors or by requirements dictated by the output windows. Nonlinear uptapers are commonly preferred over discrete steps
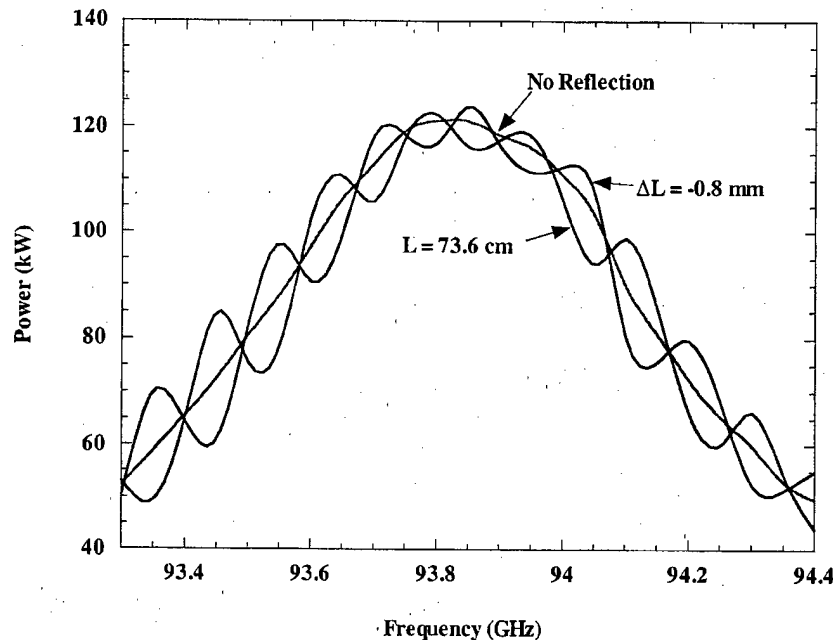
Fig. 10.   Sensitivity of bandwidth ripple to window positions. The two rippled curves have window position shifted by a quarter of an axial wavelength ($\Delta L =$ 0.8 mm). A window reflection of -20 dB and a 6 A, 65 kV, $\alpha = 1.22$ electron beam were simulated as in Fig. 7.
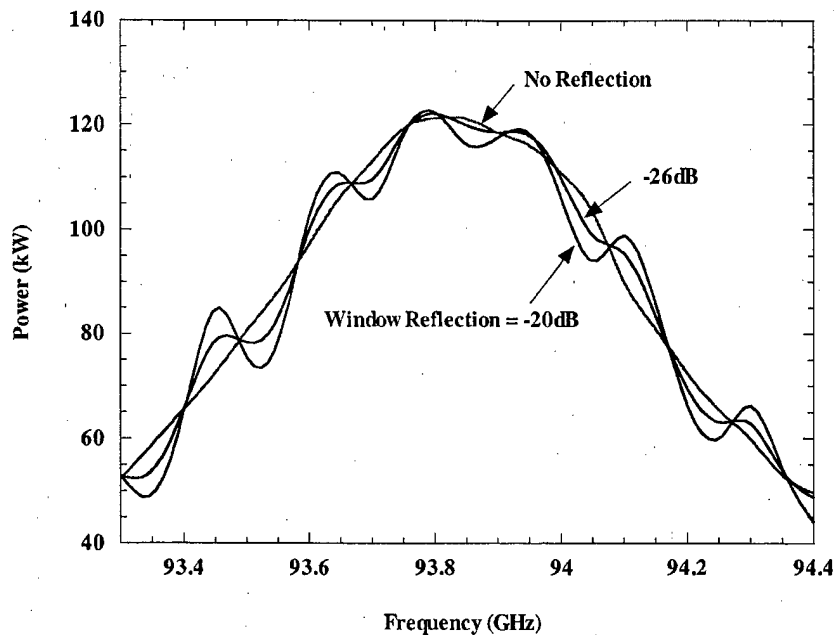

Fig. 11.   Dependence of saturated bandwidth on level of window reflection for a 6 A, 65 kV, $\alpha = 1.22$ electron beam.

or linear tapers because of minimal mode conversions, thus, ensuring high mode purity. High mode purity is critical to minimize undesirable RF absorption and reflection in the ensuing transmission line and to reduce unwanted side lobes of radiated pulses, when coupled to an antenna system.

Because of physical length constraints in most devices, all uptapers are carefully designed to maximize the mode purity with minimal length. The final optimized geometric profile of the uptaper is selected to satisfy this requirement. An example of such an optimized design is the nonlinear uptaper in the high-average

power W-band gyroklystron discussed in the previous section [Fig. 2]. This uptaper, radially shaped to follow a Dolph–Chebyshev profile, serves as the transition from the radius of the TE_{01} output cavity (~ 0.2 cm) to the radius of the beam collector (~ 1.62 cm) in a length of approximately 10 cm. The beam collector is also the output RF waveguide [10].

A more detailed picture of the operation of this uptaper can be seen in Fig. 18, which shows the geometry and the RF mode contents as a function of axial length from a MAGY simulation. The simulation was performed by exciting the output cavity with a
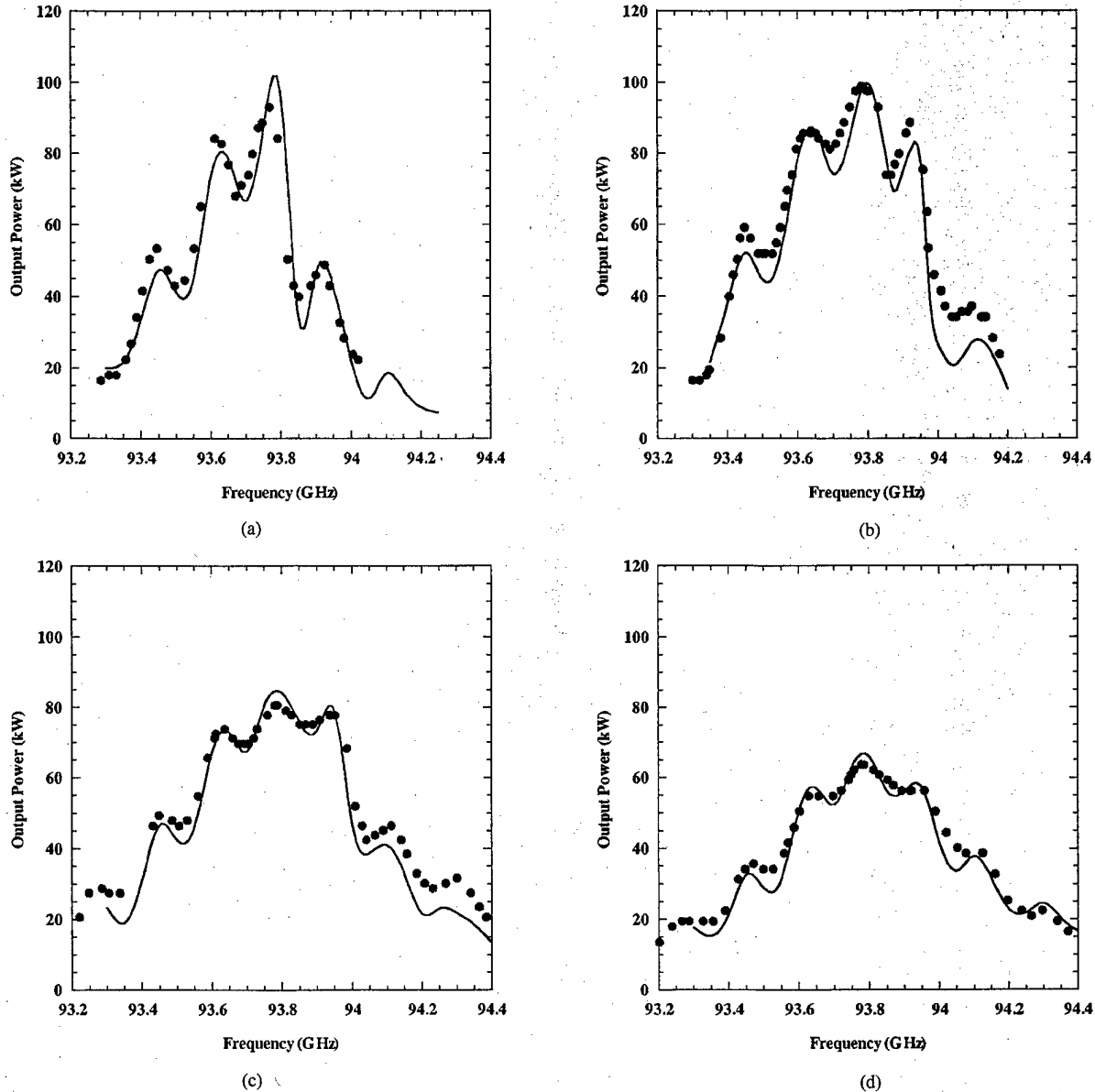
Fig. 12. Comparison between experimental bandwidth (dots) and MAGY results (solid lines) for 4-A, 65-kV beams at four different magnetic field settings. The corresponding circuit magnetic field profiles are as shown in Fig. 14. The input power and beam velocity ratio and perpendicular spread for each case are, respectively, (a) 170 W, 1.5, 4.3%, (b) 90 W, 1.55, 4.0%, (c) 250 W, 1.42, 4.6%, and (d) 340 W, 1.32, 5%.

constant RF current source, which has an axial Gaussian profile. Five different modes are included in the simulation, i.e., TE_{01}, $TE_{02}, \ldots$, and TE_{05}. As discussed previously, this is equivalent to performing a "numerical" cold test of the output cavity and the output taper. The resulting final higher order mode content of less than -37 dB from the simulation confirms the validity of the design. However, it is interesting to note the presence of substantial higher order mode within the transition [16]. For instance, the TE_{02} content can be as high as 20% before being reconverted back to the TE_{01}-mode. This process of converting the operating mode to higher order modes and then reconverting back to the operating mode to obtain high mode purity in a reasonable length is a delicate one. Consequently, it can be expected that perturbations to the RF flow within the uptaper can quickly compromise the mode purity of the RF output.

A potential major perturbation to this delicate balance is the interaction of higher order modes with the electron beam in the nonlinear uptaper. The interaction is expected to be that of the gyro-TWT type. The seed that drives these higher order mode interactions will be the power converted from the TE_{01}-mode during the transition process. For each mode, this interaction takes place approximately where the gyro-TWT resonance condition is met, i.e. the intersection between the Doppler-shifted beam line, , and waveguide dispersion line, $\omega = \Omega_c(z) + k_z(z)v_z$, and waveguide dispersion line, $\omega^2 = \omega_c^n(z)^2 + k_z(z)^2 c^2$. Here, Ω_c is the electron relativistic cyclotron frequency, ω_c^n is the cutoff frequency of the TE_{0n}-mode, and k_z is the axial wavenumber. Fig. 19 shows the cutoff frequency of several modes as a function of axial distance for this particular geometry. Also shown in the figure
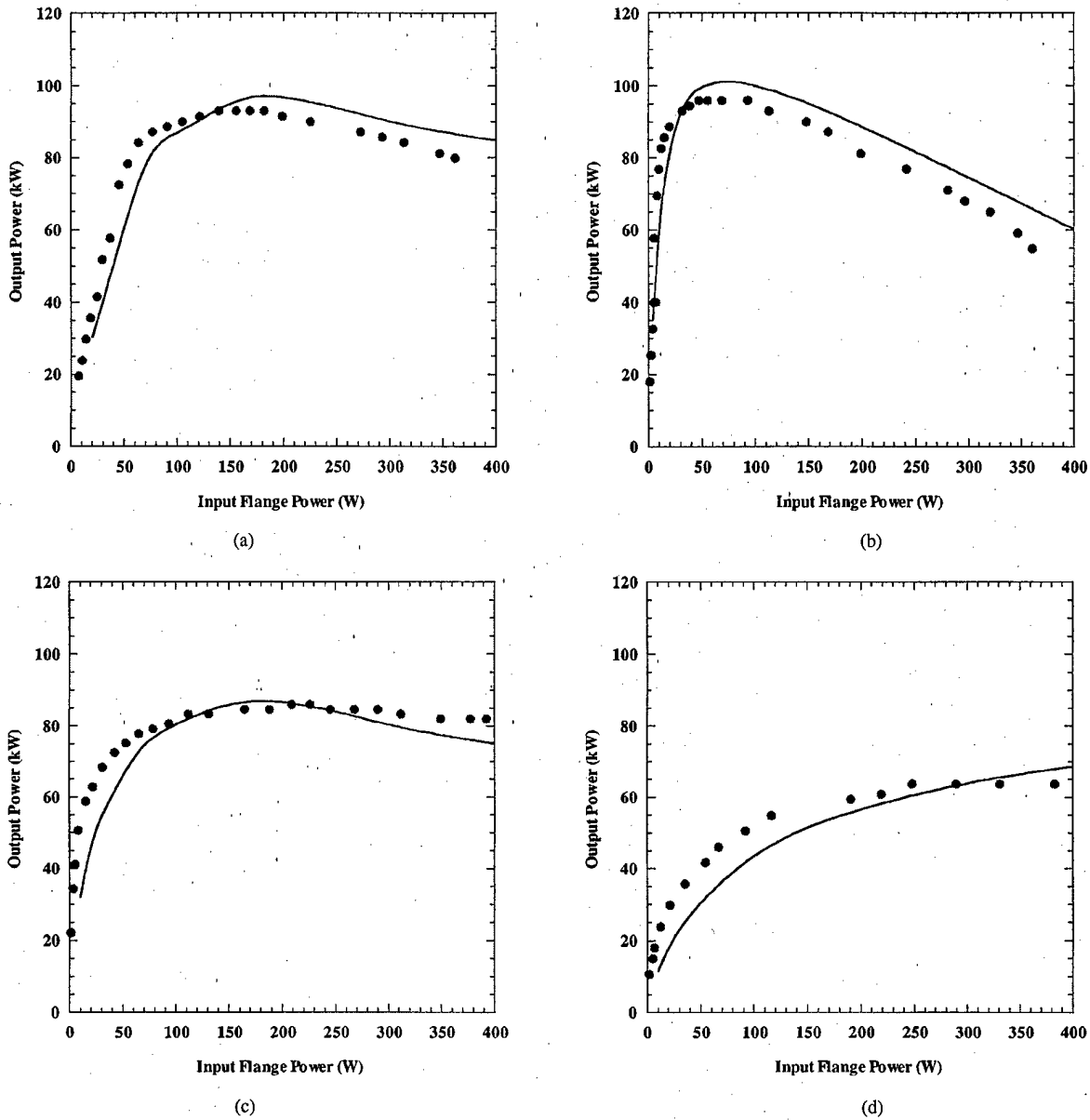
(a)

(b)

(c)

(d)

Fig. 13.   Comparison between experimental drive curves (dots) and MAGY results (solid lines) for 4-A, 65-kV beams at four different magnetic field settings. The corresponding circuit magnetic field profiles are as shown in Fig. 14. Drive frequency is 93.8 GHz for all cases. The beam velocity ratio and perpendicular spread for each case are, respectively, (a) 1.5, 4.3%, (b) 1.55, 4.0%, (c) 1.42, 4.6%, and (d) 1.32, 5%.
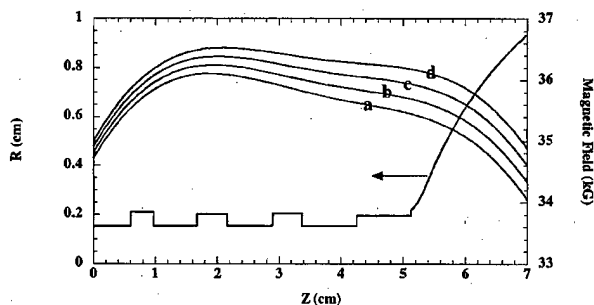

Fig. 14.   Circuit magnetic field profiles employed in MAGY simulations shown in Figs. 12 and 13. Cavity positions and dimensions are also indicated for clarity. Field profiles are calculated with magnetic field code EFFI using experimental current settings for the super-conducting coils as input.

is the line for 94 GHz for reference purposes. Assuming that the operating frequency is 94 GHz, it can be seen that higher order mode gyro-TWT interactions can only take place inside the uptaper approximately when the cutoff frequency falls below the operating frequency. Because of the rapidly changing radius of the taper, it is also expected that the interaction for each mode will only occur over a fairly short distance from where the resonance condition is first approximately satisfied.

This phenomenon is most pronounced in regimes in which the TE_{01} interaction in the output cavity is not very efficient, such as in the linear regime (low drive power) or at the bandwidth edges. This is because in such cases the beam is still energetic as it exits the output cavity and can strongly interact with higher order modes in the output taper. To quantify this phenomenon, Fig. 20 shows the
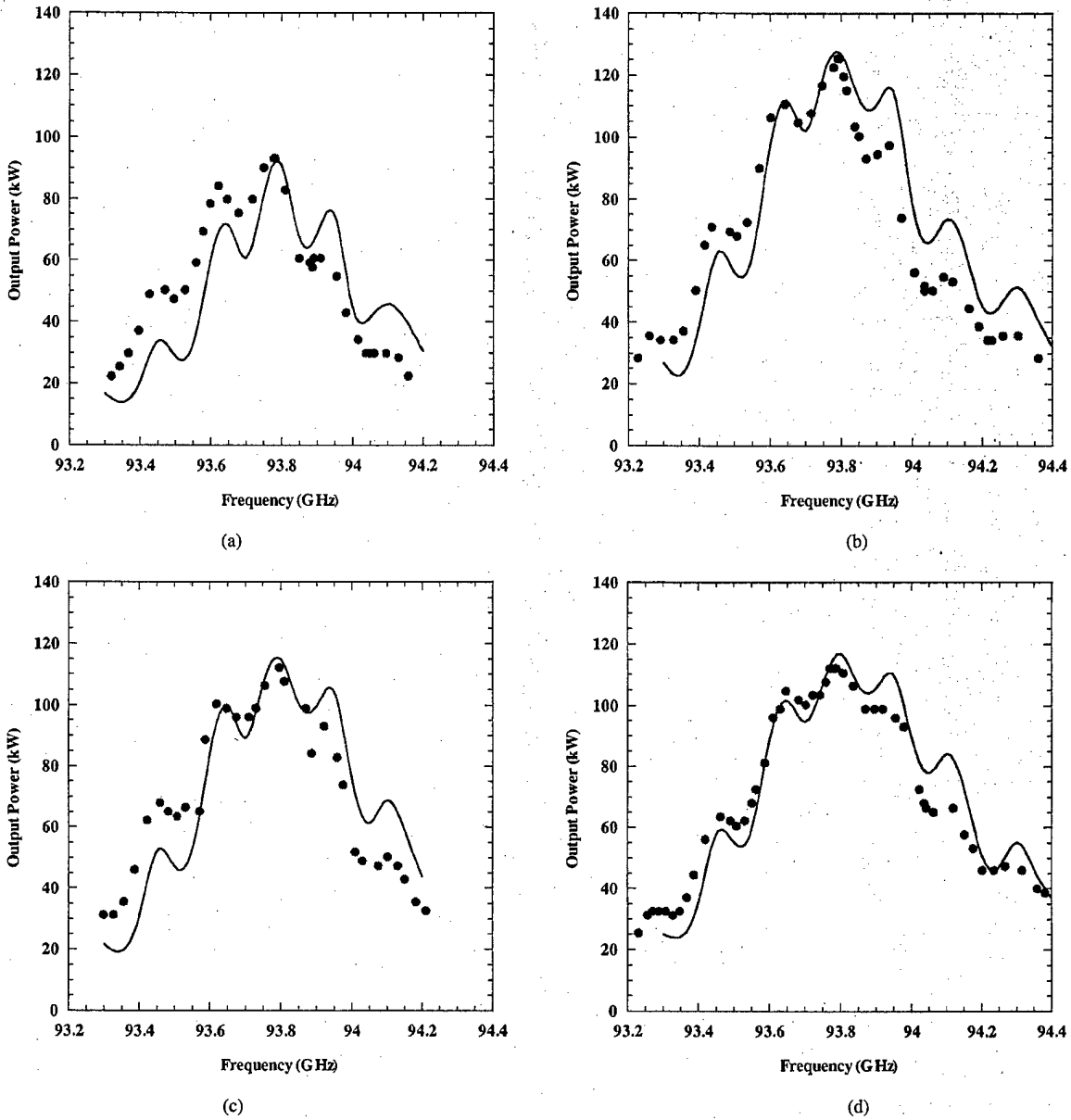
Fig. 15. Comparison between experimental bandwidth (dots) and MAGY results (solid lines) for 6-A, 65-kV beams at four different magnetic field settings. The corresponding circuit magnetic field profiles are as shown in Fig. 17. The beam velocity ratio and perpendicular spread for each case are, respectively, (a) 1.17, 5%, (b) 1.24, 4.0%, (c) 1.21, 4.5%, and (d) 1.22, 4.3%. Input power is 340 W for all cases.

total output power as well as the power distribution in higher order modes as a function of axial distance with low drive power ($\sim$0.5 W at 93.85 GHz) from a MAGY simulation. The beam current and voltage for this simulation are 6 A and 65 kV, respectively, with a pitch angle of 1.3 and no velocity spread. A uniform magnetic field of 36 kG has also been assumed. The resulting TE_{01}-mode power from the output cavity is about 1.8 kW, and it can be readily seen that the higher order modes are dominant. The total output power is 6.5 kW. It can also be seen that the lower the radial mode numbers, the closer the interaction to the output cavity, as expected. Furthermore, the higher order mode powers also peak quickly, indicating the region of synchronism for each mode is short. A similar simulation with zero input power gives zero output power. Thus, confirming that higher order mode excitation is indeed

driven by the seed provided by the mode conversion process in the output taper.

TE_{01} and higher order mode powers as a function of frequency are plotted in Fig. 21(a) at the saturation of the TE_{01}-mode (drive power is 380 W). It can be seen that in this case the higher order mode content is much reduced relative to the total output power. This is illustrated in Fig. 21(b), where the ratio of higher order mode to total output power is plotted as a function of frequency. This is because the TE_{01} interaction is efficient in robbing the beam of much of its transverse kinetic energy. Consequently, higher order mode interactions, which occur later, are much less efficient. The parameters for this particular simulation are as in the previous case but with $\alpha = 1.22$ and a realistic magnetic field.
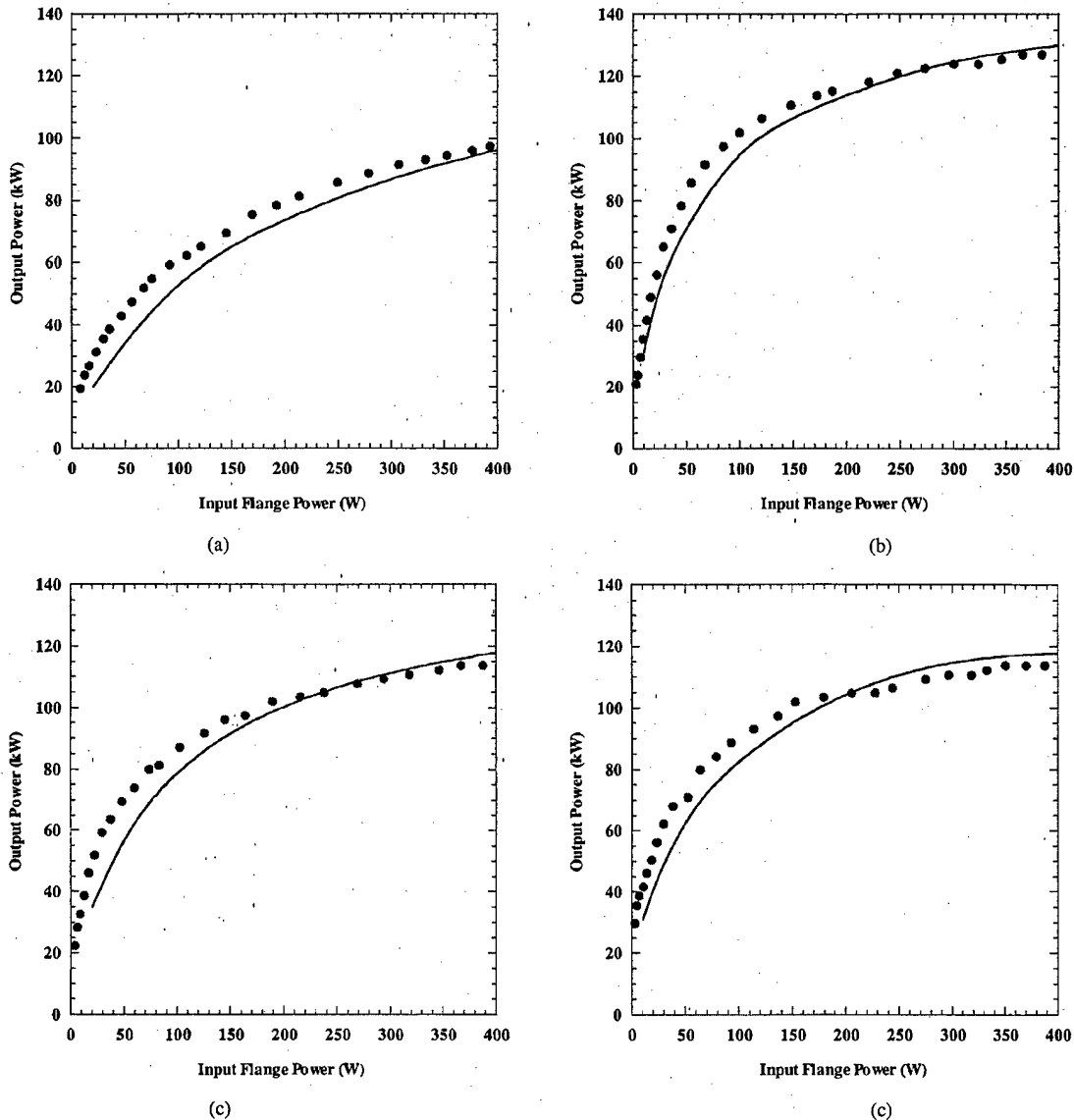
(a)

(b)

(c)

(c)

Fig. 16. Comparison between experimental drive curves (dots) and MAGY results (solid lines) for 6-A, 65-kV beams at four different magnetic field settings. The corresponding circuit magnetic field profiles are as shown in Fig. 17. The beam velocity ratio and perpendicular spread for each case are, respectively, (a) 1.17, 5%, (b) 1.24, 4.0%, (c) 1.21, 4.5%, and (d) 1.22, 4.3%. Drive frequency is 93.8 GHz for all cases.
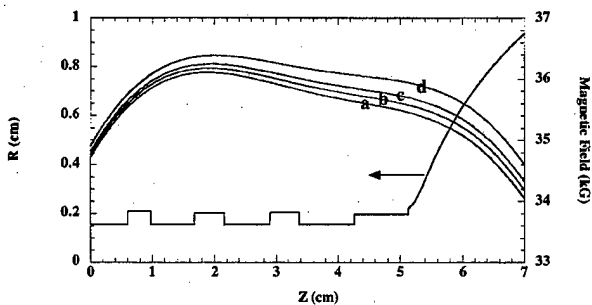

Fig. 17. Circuit magnetic field profiles employed in MAGY simulations shown in Figs. 15 and 16. Cavity positions and dimensions are also indicated for clarity. Field profiles are calculated with magnetic field code EFFI using experimental current settings for the super-conducting coils as input.
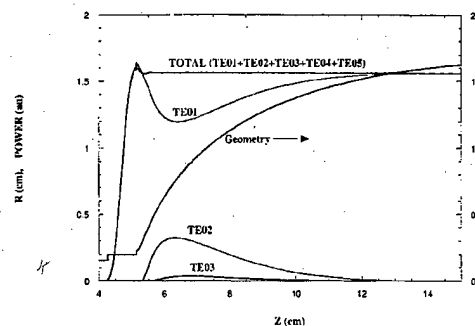
Fig. 18. Geometry of output cavity and nonlinear uptaper for the high average power W-band gyroklystron. Also shown are axial power profiles of the TE_{01}, TE_{02}, and TE_{03} modes, as well as the total power from all modes with no beam.

This study indicates that the beam–wave interaction must also be taken into account in uptaper designs to ensure high mode purity; i.e., other taper profiles can reduce the amplification of the internal higher order modes. In addition, rapid tapering of

Fig. 19.   Geometry and cutoff frequency versus axial distance. Also shown is the 94 GHz line for reference.
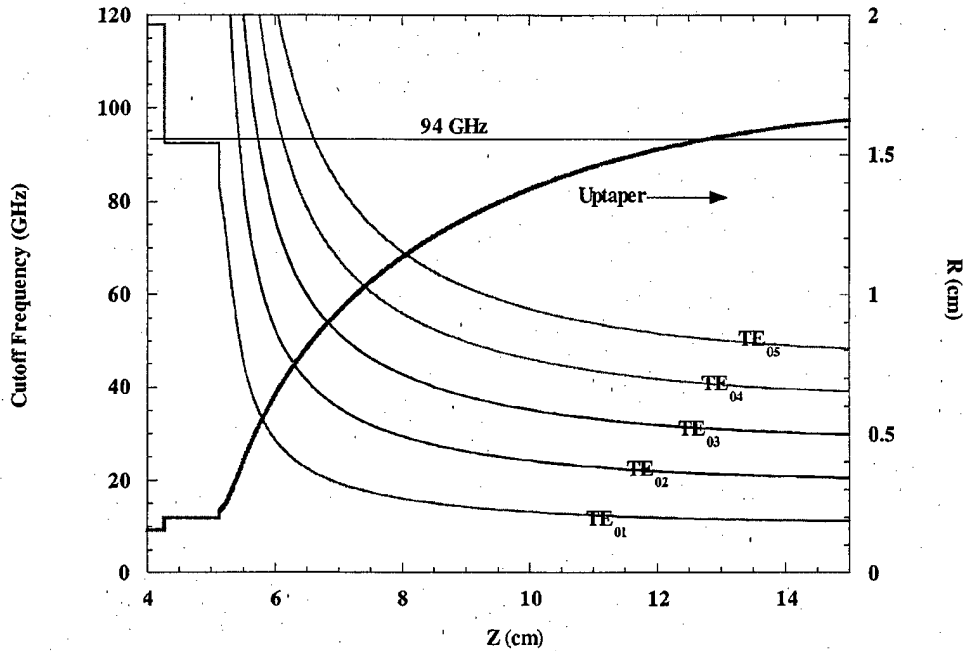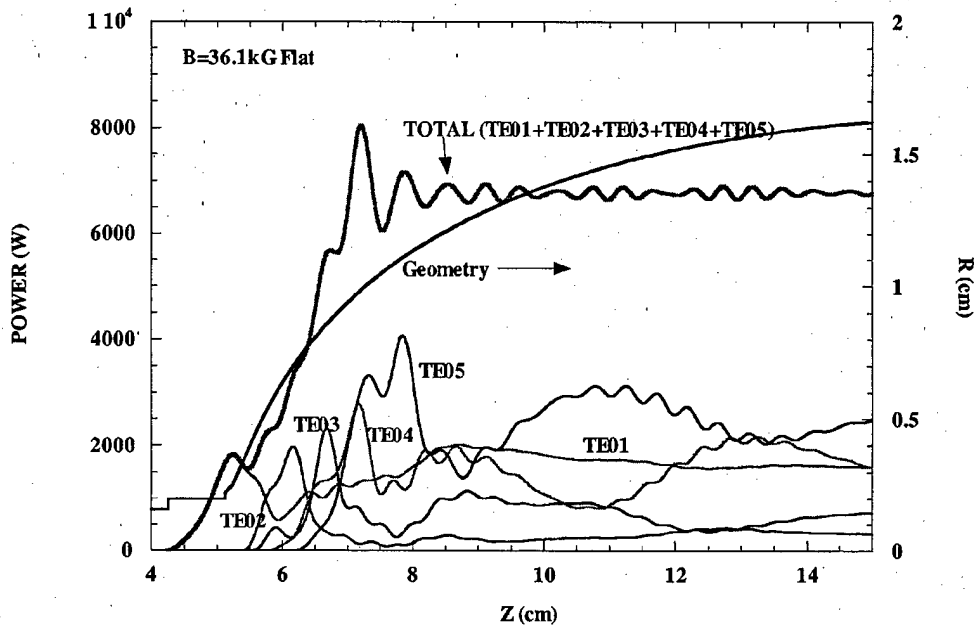

Fig. 20.   Mode contents of the output power versus axial distance in uptaper at low drive power (0.5 W at 93.85 GHz) with beam-wave interactions in uptaper. Beam current, voltage, and pitch angle are 6-A, 65-kV, and 1.3, respectively.

the magnetic field in the uptaper region can also reduce these interactions. Experimental confirmation of this phenomenon is planned.

IV. BEAM-INDUCED RF EXCITATION IN CUTOFF DRIFT SECTION

Gyroklystrons employ drift sections in part to RF isolate the cavities. These drift sections are completely cutoff to the operating mode at the operating frequency band, and they are usually lined with lossy dielectric to suppress spurious oscillations. For

instance, in the high-average power TE_{01} W-band gyroklystron, lossy dielectric linings on the drift tube wall are employed to suppress potential oscillation of modes with field distributions similar to the TE_{11}-mode in circular waveguide. In this case, the dielectric causes the field profiles to become hybrid (i.e., they have both axial magnetic and axial electric field components). However, with the appropriate choice of dielectric properties and radial thickness, the hybrid HE_{11}-, HE_{12}-, and EH_{11}-modes can be selectively loaded without seriously disturbing the cutoff properties of higher order modes and their radial field profiles
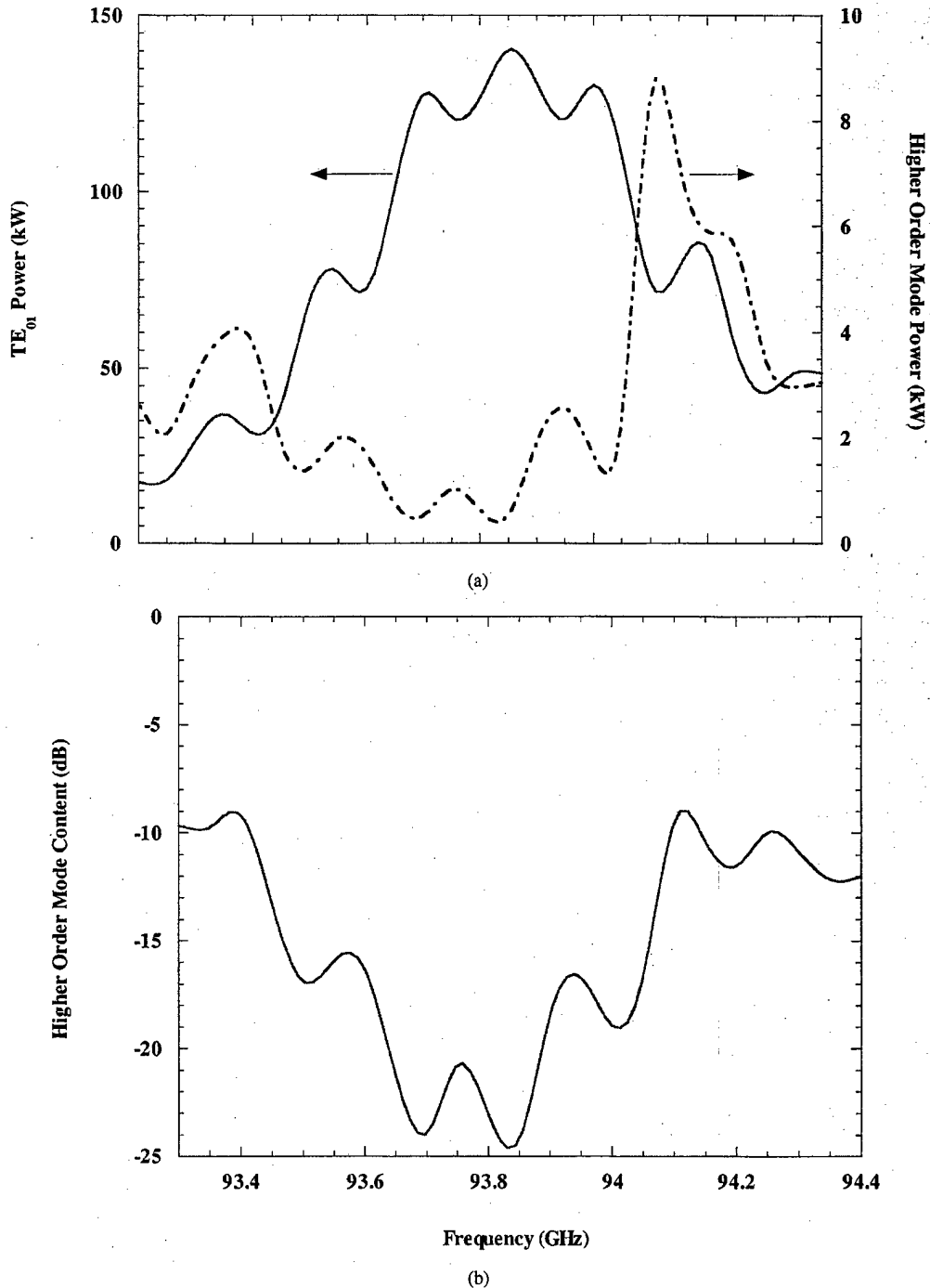
(a)

Frequency (GHz)

(b)

Fig. 21.   (a) TE_{01} (left scale) and higher order mode (right scale) powers as a function of frequency at saturation and (b) ratio of higher order mode power to total output (in dB) for a 6-A, 65-kV, $\alpha = 1.22$ beam. A reflection of -20-dB has been assumed for all modes.

(within the vacuum region of the drift tube). For a complete description of this procedure, the readers are referred to other publications [4], [17]. Because the objective of the lossy dielectric is to suppress the incipient oscillation, it is commonly expected that the RF fields will be virtually nonexistent, and thus, thermal issues will not be a serious concern even during average power operation in the design mode. Self-consistent simulations with MAGY, however, reveal that substantial RF levels can in fact be induced in these drift sections. Interestingly, the induced RF fields are found to be that of the operating mode and are at the drive frequency, which is well below cutoff. Moreover, the induced RF amplitude is found to scale linearly with the electron bunching current.

An example of this phenomenon has been alluded to earlier in connection with Fig. 2. It can be seen there that below cutoff excitation is evident in the drift section between the penultimate cavity and the output cavity, where by design the bunching current is near maximum for efficient RF extraction in the output

cavity. It is worth mentioning that the TE_{01} cutoff frequency for equivalent all-metal drift sections shown is approximately 118 GHz, and that the operating frequency (hence, the induced RF frequency) is about 93.8 GHz. Note that in the absence of the bunched beam, the RF fields for the operating mode with just the cavity excited are evanescent in these sections, as expected. However, the presence of the bunched electron beam can excite RF in a process analogous to that of a forced harmonic oscillator. The correspondence can be explained from the RF wave equation

$$\frac{1}{c^2} \frac{\partial^2 \vec{E}(t, \vec{r}, \omega)}{\partial t^2} - \nabla^2 \vec{E}(t, \vec{r}, \omega) + \frac{4\pi \sigma_s}{c^2} \frac{\partial \vec{E}(t, \vec{r}, \omega)}{\partial t}$$
$$= -\frac{4\pi}{c^2} \frac{\partial \vec{J_b}(t, \vec{r}, \omega)}{\partial t} \tag{13}$$

where $\vec{E}$ is the induced electric field in the drift section, $\vec{J_b}$ is the electron bunching current, ω is the drive angular frequency, and σ_s is the surface conductivity. Using the long axial wave-length approximation ($k_z = 0$) and defining $\hat{e}_m$ as the normalized transverse eigenvector for the mode of interest (e.g., TE_{01}), the amplitude of the electric field, E_m, is given approximately by

$$\frac{d^2 E_m(t, z, \omega)}{dt^2} + \frac{\omega_c}{Q_s} \frac{dE_m(t, z, \omega)}{dt} + \omega_c^2 E_m(t, z, \omega)$$
$$= -4\pi \int \frac{\partial \vec{J_b}(t, \vec{r}, \omega)}{\partial t} \cdot \hat{e}_m \, dA. \tag{14}$$

Here, ω_c is the cutoff frequency of the drift section, Q_s ($\sim \sigma_s^{1/2}$) represents surface loss, and the integral is over the cross section of the drift section. Equation (14) has the form of a damped forced harmonic oscillator (see, for example, [18]), for which the steady-state solution is

$$E_m(z, \omega) = \frac{-4\pi i \omega \int \vec{J_b}(z, \omega) \cdot \hat{e}_m \, dA}{\omega_c^2 - \omega^2 + i \omega \omega_c / Q_s}. \tag{15}$$

It can be readily seen here that the amplitude of the induced fields scales linearly with the electron bunching current, which explains the observable amplitude of the fields in the drift section between the penultimate cavity and the output cavity.

Two implications are associated with the nonresonant RF excitation at the drive frequency phenomenon. The first is that, strictly speaking, the usual assumption of negligible RF fields in cutoff sections or severs in amplifiers, and thus, that electrons only undergo ballistic bunching, is not correct. As shown here, the RF field amplitude can indeed be observable depending on the bunching process and how far the drive frequency is from cutoff. More importantly, for high-average power devices, the induced RF fields in the drift sections can thermally load lossy dielectric layers employed there for stability purposes. This implies that careful attention must be paid to the cooling of these dielectric layers.

In MAGY, at the present time, the expected level of thermal loading to the dielectric layers caused by nonresonant excitation is estimated from the radial component of the Poynting vector evaluated at the inner radius of the dielectric, R_d. For TE-modes, this is given by

$$P_r(\omega) = \frac{c}{8\pi} \text{ Re } \{E_\theta B_z^*\}_{r=R_d}$$
$$= \frac{c}{8\pi} \text{ Re } \{Z_s |B_z^2|\}_{r=R_d} \tag{16}$$

where $Z_s(r = R_d) = E_\theta / B_z$ is the TE-modes surface impedance for the dielectric layer. In the case when the outer radius of the layer is also the conducting wall radius, by matching the boundary conditions, the TE surface impedance in the long wavelength approximation can be shown to be

$$Z_s = \frac{E_\theta}{B_z}\bigg|_{r=R_d}$$
$$= -\frac{i}{\sqrt{\varepsilon}} \frac{H'^{(1)}_n(x_d) + \rho_{TE} H'^{(2)}_n(x_d)}{\sqrt{\varepsilon} H^{(1)}_n(x_d) + \rho_{TE} H^{(2)}_n(x_d)} \tag{17}$$

with

$$\rho_{TE} = -H'^{(1)}_n(x_w) / H'^{(2)}_n(x_w)$$
$$x_{d,w} = \sqrt{\varepsilon} \frac{\omega}{c} R_{d,w}$$

and ε is the complex dielectric constant of the layer. In these equations, $H_n^{(1)}$ and $H_n^{(2)}$ are Hankel functions, n is the azimuthal mode index number, and the prime denotes the derivative. By relating the induced axial RF magnetic field B_z to the bunching current via the wave equation

$$\nabla_\perp^2 B_z(\vec{r}, \omega) + \frac{\omega^2}{c^2} B_z(\vec{r}, \omega) = -\frac{4\pi}{c} \nabla_\perp (\vec{J_b}(\vec{r}, \omega) x \hat{e}_z) \tag{18}$$

the power loading onto the dielectric layer from the induced RF fields can be calculated according to (16).

To confirm the validity of this phenomenon, we have performed simulations with the PIC code MAGIC [19]. These simulations also reveal the existence of the below cutoff excitation phenomenon in the presence of bunched electron beam, in agreement with MAGY. Additional MAGIC simulations were performed to estimate the level of power loading on the dielectric layer. These MAGIC results have been compared with MAGY estimates using the formulation of (16) and found to be in good agreement. Consequently, (16) is presently used for estimating the thermal impact on ceramics because of this effect. A more self-consistent formulation of lossy materials, however, is being implemented in MAGY [20].

To quantify the effect of dielectric power loading from nonresonant excitation, we have applied MAGY to one of the W-band gyroklystrons at NRL [21]. The geometry and RF field profile (at saturation) are as shown in Fig. 22. In fact, this gyroklystron is the prototype for the high-average power gyroklystron [3], [4]. This prototype, as in the high-average
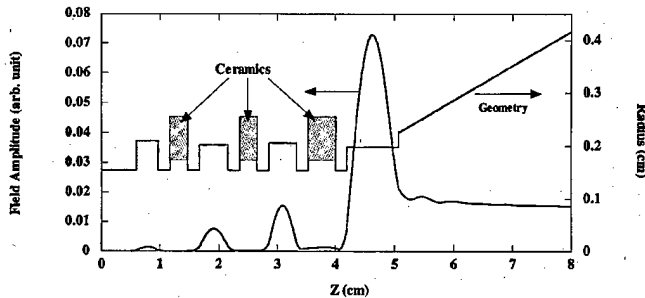
Fig. 22. Geometry and RF field profile for one of NRL W-band gyro-klystron. Operating mode drift tube cutoff frequencies are approximately 118 and 104 GHz in metal and dielectric loaded sections, respectively.
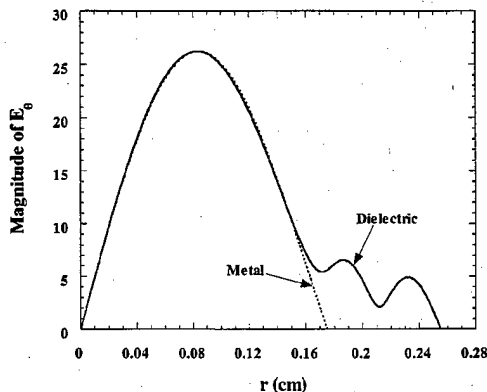

Fig. 23. Comparison of operating mode radial electric field profiles in drift sections with and without the dielectric lining at 93.8 GHz. The metal wall radius is 0.175 cm. The dielectric (a composite of 80% BeO and 20% SiC by weight) inner radius and thickness are 0.175 and 0.08 cm, respectively. Cutoff frequency is 0.3% lower with the dielectric lining.
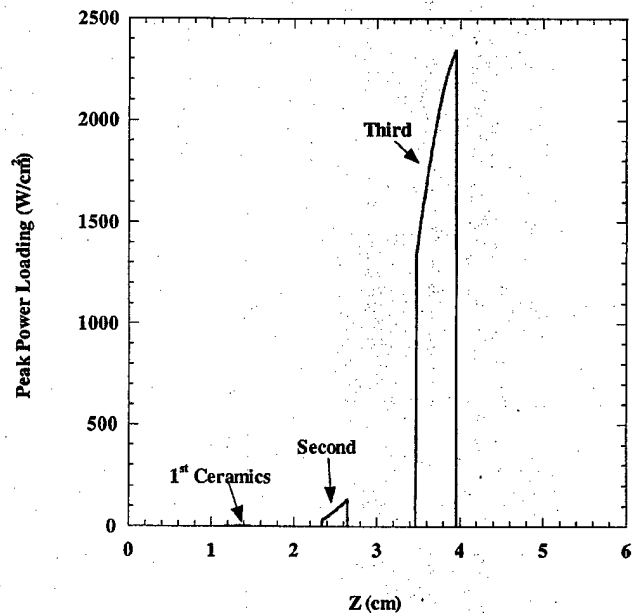

Fig. 24. Peak power loading on the ceramics shown in Fig. 22.

of 11%. At this level of average power loading, the ceramics will fail unless they are aggressively cooled. Subsequent to this analysis, a detailed thermal analysis of the last ceramics in the high-average power device has been performed. The analysis indicates that a moderate temperature rise of 25 °C relative to the cooled metal wall can be achieved assuming good thermal contact between the ceramics and the cooled metal wall.

V. CONCLUSION

power version [4], employs dielectric loading in each of the three drift sections to suppress spurious oscillations. The dielectrics are a composite of 80% BeO and 20% SiC by weight with a complex dielectric constant $\varepsilon = 12.24 - i3.67$ (at $\sim$94 GHz). The dielectric inner radius and thickness are 0.175 and 0.08 cm, respectively. The lengths are 0.3 cm, except for the one in between the penultimate and output cavities, which is 0.48 cm long. With this configuration of dielectric loading in the drift tube, there is minimal effect on the field profile and cutoff behavior of the operating mode, which is similar to the TE_{01} in the vacuum region and has a small tail that leaks into the dielectric, as illustrated in Fig. 23. At 93.8 GHz, the radial shift in the vacuum field profile maximum is only about 0.3%, with an equal percentage change in the effective wall radius (resulting in a cutoff frequency of 104 GHz). This is negligible, justifying the use of the metal drift tube with unchanged dimensions and an effective finite conductivity. The peak power loading on the ceramics as calculated by MAGY for a 6 A, 65 kV, $\alpha = 1.5$ at saturation is shown in Fig. 24. As expected, the loading is highest for the last dielectric layer because the electron bunching current is near maximum there. The induced RF field at this position is indeed observable, as can be seen in Fig. 22.

For high-average power operation, the highest peak power loading of 2.4 kW/cm² [Fig. 24] translates into an average power loading as high as 264 W/cm², assuming a duty cycle

In this paper, the self-consistent capability of MAGY is being employed to investigate several issues relating to gyroklystrons. The effects of window reflections on the performance of gyroklystrons were presented. It was shown that window reflection could induce bandwidth power ripple. The amplitude of which depends strongly on the reflection coefficient, and the ripple frequency spacing is a function of the geometry of the waveguide between the output cavity and the reflector. Furthermore, window reflections also result in output phase ripple across the band and modify the output cavity diffractive quality factor Q_{diff}. This modification of Q_{diff} can significantly impact the start oscillation current threshold of the output cavity. The excellent correlation between experimental data and simulation results indicates that the observed ripple in the bandwidth of the high-average power W-band gyroklystron [3], [4] can indeed be attributed to a small -20-dB reflection from the window. Simple scaling laws are also developed, which allow for a quick estimation of the impact on the gyroklystron performance for a given window reflection. The potential for higher order mode excitations in nonlinear output tapers is also discussed. The higher order mode interactions are that of the gyro-TWT type with the initial drive power for each mode provided by the internal mode conversion in the taper. This effect can compromise mode purity of the output RF for which the use of output tapers is intended to minimize.

It is most pronounced in at low drive power or at the bandwidth edges where the operating mode interaction in the output cavity is not very efficient. This suggests that designs of output taper should take into account possible beam–wave interactions to ensure that high mode purity is indeed achieved. Finally, nonresonance excitation in cutoff drift sections driven by the bunched electron beam was also presented. The induced RF fields are found to be that of the operating mode and are at the drive frequency, which is well below cutoff. The RF amplitude scales linearly with that of the electron bunching current. This phenomenon is similar to that of a forced harmonic oscillator. The presence of induced RF in drift sections can potentially impact the use and design of lossy ceramics employed in these sections for stability purposes, particularly, in high-average power devices where thermal issues are a major concern.

Even though the work presented here focus exclusively on gyroklystrons, MAGY has also been applied to gyro-TWT designs. The results of gyro-TWT modeling will be presented in a future publication.

REFERENCES

[1] M. Botton, T. M. Antonsen, Jr., B. Levush, K. T. Nguyen, and A. N. Vlasov, "MAGY: A time-dependent code for simulation of slow and fast microwaves devices," IEEE Trans. Plasma Sci., vol. 26, p. 882, June 1998.

[2] V. L. Bratman, M. A. Moiseev, M. I. Petelin, and R. E. Erm, "Theory of gyrotron with a nonfixed structure of the high-frequency field," Radiophys. Quantum Electron., vol. 16, p. 474, 1973.

[3] M. Blank, B. G. Danly, B. Levush, J. P. Calame, K. Nguyen, D. Pershing, J. Petillo, T. A. Hargreaves, R. B. True, A. J. Theiss, G. R. Good, K. Felch, B. G. James, P. Borchard, P. Cahalan, T. S. Chu, H. Jory, W. G. Lawson, and T. M. Antonsen, Jr., "Demonstration of a 10 kW average power 94 GHz gyro-klystron amplifier," Phys. Plasmas, vol. 6, p. 4405, 1999.

[4] B. G. Danly, M. Blank, J. P. Calame, B. Levush, K. T. Nguyen, D. Pershing, R. K. Parker, K. L. Felch, B. G. James, P. Borchard, T. S. Chu, H. R. Jory, T. A. Hargreaves, R. B. True, W. G. Lawson, and T. M. Antonsen, Jr., "Development and testing of a high average power, 94 GHz gyroklystron," IEEE Trans. Plasma Sci., vol. 28, pp. 713–726, June 2000.

[5] M. Kuntze, E. Borie, G. Dammertz, B. Piosczyk, and M. Thumm, "140 GHz gyrotron with 2.1 MW output power," in Proc. 24th Int. Conf. Infrared Millimeter Waves, vol. W-A6, L. A. Lombardo, Ed., Monterey, CA, Sept. 1999.

[6] T. M. Antonsen, Jr., S. Y. Cai, and G. S. Nusinovich, "Effect of window reflection on gyrotron operation," Phys. Fluids B, vol. 4, p. 4131, 1992.

[7] G. Dammertz, O. Braz, M. Kuntze, B. Piosczyk, and M. Thumm, "Influence of window reflections on gyrotron operation," in Proc. 22th Int. Conf. Infrared Millimeter Waves, H. P. Freund, Ed., Wintergreen, VA, July 1997, p. 150.

[8] M. Yu. Glyavin and V. E. Zapevalov, "Reflection influence on gyrotron operation regime," Int. J. Infrared Millimeter Waves, vol. 19, p. 1499, 1998.

[9] P. Muggli, M. Q. Tran, T. M. Tran, H.-G. Matthews, G. Agosti, S. Alberti, and A. Perrenoud, "Effect of power reflection on the operation of a low-Q 8 GHz gyrotron," IEEE Trans. Microwave Theory Tech., vol. 38, p. 1345, 1990.

[10] K. T. Nguyen, B. G. Danly, B. Levush, M. Blank, R. True, G. R. Good, T. A. Hargreaves, K. Felch, and P. Borchard, "Electron gun and collector design for 94 GHz gyro-amplifiers," IEEE Trans. Plasma Sci., vol. 26, p. 799, June 1998.

[11] D. E. Pershing, A. H. McCurdy, B. G. Danly, J. M. Cameron, and M. Blank, "Dielectric probe development for W-band gyro-klystron cavity testing," in Proc. 24th Int. Conf. Infrared Millimeter Waves, vol. W-D3, L. A. Lombardo, Ed., Monterey, CA, Sept. 1999.

[12] W. B. Herrmannsfeldt, "Electron trajectory program," SLAC, Stanford, CA, Rep. 226, 1979.

[13] S. J. Sackett, "Users manual for EFFI," Lawrence Livermore Nat. Lab., Livermore, CA, vol. UCID-17 621, 1981.

[14] P. E. Latham, W. G. Lawson, and V. Irwin, "The design of a 100 MW Ku-band second harmonic gyro-klystron experiment," IEEE Trans. Plasma Sci., vol. 22, p. 804, Oct. 1994.

[15] W. G. Lawson, "Theoretical evaluation of nonlinear tapers for a high-power gyrotron," IEEE Trans. Microwave Theory Tech., vol. 38, p. 1617, Nov. 1990.

[16] A. Mobius and M. Thumm, "Gyrotrons output launchers and output tapers," in Gyrotron Oscillators: Their Principles and Practice, C. J. Edgecombe, Ed. Bristol, PA: Taylor and Francis, 1993.

[17] B. Levush, M. Blank, J. Calame, B. Danly, K. Nguyen, D. Pershing, S. Cooke, P. Latham, J. Petillo, and T. Antonsen, Jr., "Modeling and design of millimeter wave gyroklystrons," Phys. Plasmas, vol. 6, p. 2333, 1999.

[18] K. R. Symon, Mechanics. Reading, MA: Addison-Wesley, 1971.

[19] B. Goplen, L. Ludeking, and D. Smithe, MAGIC User's Manual, Mission Res. Corp., Newington, VA, vol. MRC/WDC-R-380, Oct. 1996.

[20] A. Vlasov and T. Antonsen, Jr., "Numerical solution of fields in lossy structures using MAGY," in Proc. 24th Int. Conf. Infrared Millimeter Waves, vol. W-D6, L. A. Lombardo, Ed., Monterey, CA, Sept. 1999.

[21] M. Blank, B. G. Danly, B. Levush, and D. E. Pershing, "Experimental investigation of W-band (94 GHz) gyroklystron amplifiers," IEEE Trans. Plasma Sci., vol. 26, p. 409, June 1998.

Khanh T. Nguyen received the B.S. degree in physics and mathematics in 1978, the M.S. degree in mathematics in 1979, and the M.S. and the Ph.D degrees in nuclear science in 1980 and 1983, respectively, all from the University of Michigan, Ann Arbor. His Ph.D research topic was a stability study of the ELMO Bumpy Torus Fusion Device.

He then joined the Department of Research and Technology, Naval Surface Warfare Center, White Oak, where he was the Lead Theorist for the charged particle beam propagation experimental program. In 1989, he joined the Washington Office of Mission Research Corporation as a Senior Scientist, and later became the leader of the Electromagnetic Application Group. At MRC, his research efforts were in the areas of charged particle beam propagation, vacuum electronics, compact accelerator development, x-ray and g-ray simulators, and high-power microwave sources development. Since 1994, when he initiated KN Research, he has been an on-site contractor with the Vacuum Electronics Branch, Naval Research Laboratory. His current research emphasis is on the design and modeling of vacuum electronic devices.

Baruch Levush (M'88–SM'90) received the M.Sc. degree in physics from Latvian University, Riga, Latvia, in 1972 and the Ph.D. degree in physics from Tel-Aviv University, Tel-Aviv, Israel, in 1981.

He received the Dr. Ch. Weizman Postdoctoral Fellowship and stayed for two years at the University of Maryland, College Park. From 1984 to 1985, he was a Research Scientist with Rafael Research Laboratory, Israel. In 1985, he joined the University of Maryland, where his research was focused on the physics of coherent radiation sources and the design of high-power microwave sources, such as gyrotrons, TWT's, BWO's, and free electron lasers. In 1993, he became a Senior Research Scientist at the Institute for Plasma Physics, University of Maryland. In 1995, he joined the Naval Research Laboratory, Washington, DC, as the Head of the Theory and Design Section of the Vacuum Electronics Branch. He is actively involved in developing theoretical models and computational tools for analyzing the operation of existing microwave vacuum devices and in inventing new concepts for high-power, high-frequency coherent radiation sources. He is the author and coauthor of more than 100 journal articles.

Dr. Levush is a Member of the American Physical Society.

Thomas M. Antonsen, Jr. (M'87) was born in Hackensack, NJ in 1950. He received the Bachelor's degree in electrical engineering in 1973, and his Master's and Ph.D. degrees in 1976 and 1977, all from Cornell University. He was a National Research Council Post Doctoral Fellow at the Naval Research Laboratory in 1976–1977, and a Research Scientist in the Research Laboratory of Electronics at MIT from 1977 to 1980. In 1980, he moved to the University of Maryland where he joined the faculty of the departments of Electrical Engineering and Physics in 1984. He is currently a Professor of Physics and Electrical Engineering. He has held visiting appointments at the Institute for Theoretical Physics (U.C.S.B.), the Ecole Polytechnique Federale de Lausanne, Switzerland, and the Institute de Physique Theorique, Ecole Polytechnique, Palaiseau, France. He was selected as a Fellow of the Division of Plasma Physics of the American Physical Society in 1986.

Prof. Antonsen's research interests include the theory of magnetically confined plasmas, the theory and design of high power sources of coherent radiation, nonlinear dynamics in fluids, and the theory of the interaction of intense laser pulses and plasmas. He is the author and coauthor of more than 180 journal articles and coauthor of the book *Principles of Free-electron Lasers*. He has served on the editorial board of Physical Review Letters. The Physics of Fluids, and Comments on Plasma Physics.

Moti Botton, photograph and biography not available at the time of publication.

Monica Blank received the B.S. degree (electrical engineering) from the Catholic University of America, Washington, DC, in 1988, and the M.S. and Ph.D. degrees (electrical engineering) in 1991 and 1994, respectively, from the Massachusetts Institute of Technology, Cambridge, where her dissertation work involved theoretical and experimental studies of quasi-optical mode converters for high power gyrotron oscillators.

In 1994 she joined the Vacuum Electronics Branch of the Naval Research Laboratory, where she was responsible for the design and demonstration of high-power millimeter wave vacuum electronic devices for radar applications. In 1999 she joined the gyrotron team at Communications and Power Industries (formerly Varian) where she continues her work on high-power millimeter wave gyrotron amplifiers.

J. P. Calame (M'96) received the B.S. degree in 1985, the M.S. degree in 1986, and the Ph.D. degree in 1991, all in electrical engineering, from the University of Maryland, College Park.

He performed part-time research on the electrical behavior of ionic crystals and ion-conducting polymers at the U.S. Naval Academy Physics Department, Annapolis, MD, from 1980 to 1985. His graduate research from 1985 to 1991 involved the development of high peak power gyroklystrons. From 1991 to 1992, he worked with microfabricated field emission electron sources and devices at the Naval Research Laboratory, Washington, DC. From 1992 to 1997, he studied high-power microwave amplifiers, the microwave processing of materials, and the dielectric properties of ceramics at the Institute for Plasma Research, University of Maryland. Presently, he is with at the Naval Research Laboratory, where he is developing high average power, wideband millimeter-wave amplifiers for radar applications. He is also studying the dielectric and thermal properties of composite ceramic materials, and he is investigating intrinsic electronic noise in millimeter-wave systems.

Dr. Calame received the 1991 APS award for Outstanding Doctoral Thesis Research in Beam Physics.

Bruce G. Danly (M'87) received the B.A. degree in physics from Haverford College, and the Ph.D. degree in physics from the Massachusetts Institute of Technology, in 1978 and 1983, respectively. His doctoral dissertation in the area of quantum electronics was on high power infrared Raman lasers. From 1983 to 1995.

He was on the research staff at the MIT Plasma Fusion Center, first as Research Scientist from 1983–1992, and then as Principal Scientist from 1992–1995. While at MIT, he participated in research on gyrotrons, free-electron lasers, relativistic klystrons, and other high power RF source technologies for use in plasma heating and high-gradient RF linear accelerators. In 1995, he joined the Naval Research Laboratory as Head of the High Power Devices Section, Vacuum Electronics Branch. The high power devices section carries out experimental research and development on new concepts for high power microwave, millimeter wave, and infrared sources based on both slowwave and fastwave interaction mechanisms. Technologies under investigation include the class of gyrotron amplifiers (gyroklystrons, gyrotwystrons, gyro-TWT's), free-electron lasers, TWT's, and klystrons. In addition to his duties as head of the High Power Devices Section, he is also the Program Point of Contact for the High Performance Millimeter Wave Devices Program, administered by the NRL Vacuum Electronics Branch for the Office of Naval Research. This program carries out exploratory development of new high power amplifiers in the millimeter wave bands, in particular the Ka- and W-Bands.

Dr. Danly is a member of the APS and Divisions of Physics of Beams and Plasma Physics.